

Determining the modal mineralogy of mafic and ultramafic igneous rocks using thermal emission spectroscopy

Victoria E. Hamilton and Philip R. Christensen

Department of Geology, Arizona State University, Tempe

Abstract. The modal mineralogies of 20 mafic and ultramafic igneous rocks were determined from their thermal infrared emission spectra using a linear deconvolution approach, which uses a library of end-member mineral spectra to model a bulk rock spectrum. Over 90% of the modes obtained from thermal emission spectra agree with modes obtained by traditional optical analyses to within the stated error of the optical analyses (5–15 vol %). Library spectra of several compositions within a solid solution series (e.g., plagioclase feldspars labradorite and bytownite) were commonly used in each best fit model and are assumed to represent, in combination, a composition in the rock for which an identical mineral spectrum was unavailable in the library. The accuracy of this assumption was evaluated by calculating a weighted average solid solution composition for plagioclase and/or pyroxenes from the library minerals used in the model best fit of 14 rocks and comparing these compositions to the actual chemistries measured by electron microprobe or the optically estimated An#. The derived solid solution compositions are generally within 10–15 An# (or Mg#) of the measured composition. Modal data derived from the spectra via the deconvolution were summed and converted to weight percent (wt %) oxides for comparison to standard bulk chemistry data. SiO₂, Al₂O₃, and Na₂O + K₂O were generally slightly overestimated, and FeO and MgO were typically slightly underestimated. Modes and wt % oxides were plotted on standard rock type classification diagrams and provide broadly accurate classifications, demonstrating that the linear deconvolution technique is successful at deriving useful mineralogical information from thermal infrared emission spectra of bulk rock samples. Furthermore, convolution of the laboratory data to spectral resolutions comparable to remote sensing instruments (specifically, the Mars Global Surveyor Thermal Emission Spectrometer) demonstrates only a ~5 vol % increase in modal uncertainty for minerals present in abundances ≥10 vol %. This study thus provides a strong foundation for the application of this technique to mafic igneous sample spectra from both laboratory and remote sensing instruments.

1. Introduction

There are several compelling reasons to study the infrared emission spectra of bulk rock samples and the determination of modal mineralogy from those spectra. From a laboratory perspective, traditional bulk sample analysis techniques commonly require sample preparation (e.g., thin sectioning) and/or long analysis times (e.g., petrographic analysis, electron microprobe analysis, shipping to outside labs). The ability to analyze an unprepared rock sample in under 1 hour, including obtaining modal mineral abundances on a par with optical methods, could potentially save a great deal of time during the course of a research project. With the increasing availability of thermal infrared remote sensing data, a comprehensive understanding of emission spectra in particular is desirable to extract the greatest possible amount of chemical information about the observed surface.

Examination of the thermal infrared spectra of igneous rocks is not new and has been performed by numerous authors. Lyon [1965] established that measurements of rough rock surfaces could be made directly using the emission technique and observed that linear combinations of the appropriate mineral

spectra mimicked the spectral signatures of the rocks. Vincent and Thomson [1972] devised a scheme for estimating silica contents from a ratio of the average radiance in two strong silicate reststrahlen bands, and Walter and Salisbury [1989] developed a technique for relating the radiance in key bands to a chemical index referred to as “SCFM.” A study by Hamilton *et al.* [1997] used linear deconvolution [Ramsey, 1996; see also Ramsey and Christensen, 1998] to determine the modal mineralogy of several Martian meteorites from their infrared spectra, and Feely and Christensen [1999] applied linear deconvolution to the emission spectra of 96 igneous and metamorphic lithologies. The linear deconvolution technique is applied in the present work as well.

Linear deconvolution provides a method for separating the infrared spectrum of a rock into its constituent minerals, presenting the results in terms of modal mineral abundances, which then may be applied to the general lithologic classification of unknown samples [Ramsey, 1996; Hamilton *et al.*, 1997; Feely and Christensen, 1999]. Deconvolution of thermal infrared rock spectra is based on the principle that the energy emitted from a rock surface is equivalent to the linear addition of the emitted energy of each component mineral in proportion to its observed areal percentage. The assumption of linearity is made possible by the high absorption coefficients in rock and coarse particulate samples that minimize nonlinear

Copyright 2000 by the American Geophysical Union.

Paper number 1999JE001113.
0148-0227/00/1999JE001113\$09.00

Table 1. Rock Sample Data

Sample	Rock Type	Location	Bulk Analysis	Optical Analysis	Microprobe Analysis	Volcanic/ Plutonic	Zone
RSL-11-94-2	Olivine subalkali basalt	Shaw Butte, Ariz.	no	yes	partial	volcanic	N/A
RSL-12-94-8	Basaltic andesite	Sycamore Canyon, Ariz.	yes	yes	no	volcanic	N/A
RSL-4-95-23	Olivine subalkali basalt	Lincoln Springs, Ariz.	yes	yes	no	volcanic	N/A
RSL-9-94-12	Basaltic andesite	Black Mtn., Ariz.	yes	yes	partial	volcanic	N/A
RSL-9-94-36	Basaltic andesite	Gillespie Dam, Ariz.	yes	yes	no	volcanic	N/A
RSL-9-94-41	Olivine subalkali basalt	Hot Rock Mtn., Ariz.	yes	yes	partial	volcanic	N/A
RSL-9-94-42	Basaltic andesite	Hot Rock Mtn., Ariz.	yes	yes	no	volcanic	N/A
STL-5	Gabbronorite	Stillwater Complex, Mont.	yes	yes	yes	plutonic	Gabbronorite II
STL-20	Norite	Stillwater Complex, Mont.	yes	yes	yes	plutonic	Gabbronorite III
STL-50	Gabbronorite	Stillwater Complex, Mont.	yes	yes	yes	plutonic	Gabbronorite III
STL-100	Gabbronorite	Stillwater Complex, Mont.	yes	yes	yes	plutonic	Gabbronorite I
STL-138	Gabbronorite	Stillwater Complex, Mont.	yes	yes	yes	plutonic	Gabbronorite I
WAR-R0039	Augite basalt porphyry	unknown	yes	yes	no	volcanic	N/A
WAR-R0519	Olivine pyroxene andesite	unknown	yes	yes	no	volcanic	N/A
WAR-R1049	Deccan basalt	Bombay, India	yes	yes	no	volcanic	N/A
WAR-R1079	Olivine basalt porphyry	Helena, Mont.	yes	yes	no	volcanic	N/A
WAR-R2624	Diabase	Jersey City, N. J.	yes	yes	no	plutonic	N/A
WAR-R3309	Gabbro	Duluth, Minn.	yes	yes	no	plutonic	N/A
WAR-R3319	Norite	Sudbury, Ontario	yes	yes	no	plutonic	N/A
WAR-R6479	Harzburgite	Nye, Mont.	yes	yes	no	plutonic	N/A

N/A, not available.

multiple scattering of energy. A linear least squares deconvolution technique thus may be used to derive the percentages of constituent minerals and their compositions from rock spectra [Thomson and Salisbury, 1993; Ramsey and Christensen, 1998].

The present study attempts to build primarily on the work of Feely and Christensen [1999] in several ways. The results of that study showed that the modeled modes of major minerals (feldspar, pyroxene, quartz, and calcite/dolomite) in each rock were accurate to within ± 6 –14 vol %, depending on the mineral; minor minerals such as hornblende and micas exhibited slightly higher errors, ranging from ± 10 to 13 vol %, depending on the mineral [Feely and Christensen, 1999]. Aside from discussion of errors associated with the linear deconvolution technique itself, only a limited discussion of the mineralogical sources of errors in mineral modeling was presented by the authors, and no comparisons to solid solution mineral compositions in the rocks were performed, nor were the modeled modes compared collectively such that estimates of errors in rock type classification could be made. In the present work, modeled modes are compared to optically estimated modes, the model-derived effective compositions of solid solution series minerals are compared to measured mineral compositions, and the modes and compositions of the modeled end-members are used to generate wt % oxides for comparison with bulk chemical data for each rock. Derived modes (and wt % oxides) are then used to classify each rock and compared to the classification obtained based on the optical or bulk analysis. Thus the objective of this work is to determine the accuracy of linear deconvolution in fitting not only the proper minerals to a rock spectrum, but also in modeling solid solution compositions (specifically, pyroxene and plagioclase feldspar). The accuracy of the determined mineralogy impacts the use of these data for classification of rocks both in the laboratory and from remote sensing data.

2. Samples and Data Acquisition

2.1. Sample Descriptions

The 20 igneous rock samples studied in this work consist of intrusive and extrusive textures, mafic and ultramafic compo-

sitions, and are all pyroxene-bearing compositions (having varying proportions of orthopyroxene and clinopyroxene) as a link to and a test of results from a companion study [Hamilton, this issue]. Table 1 provides a listing of all samples, their rock type classification, and additional information and characteristics of interest.

Our data represent two types of physical samples: (1) cut surfaces, ideally comparable to unweathered and/or particulate surfaces (e.g., sand) that would not normally exhibit weathering rinds, and (2) natural surfaces. Rocks analyzed on cut surfaces include specimens with sample numbers beginning STL- or WAR-. The STL samples are from the Gabbronorite I, II, and III zones of the Stillwater Complex, Montana, provided by I. S. McCallum of the University of Washington (see McCallum [1996] for a review of the geology of the Stillwater Complex). These samples all consist of predominantly three minerals in varying proportions (orthopyroxene, clinopyroxene, and plagioclase feldspar) with variable solid solution compositions. The WAR samples are a diverse collection from many localities purchased from Ward's Natural Science Establishment. The natural surfaces of a suite of basalts and basaltic andesites from central Arizona comprise the second group of samples (sample numbers beginning RSL-) and demonstrate the efficacy of the deconvolution technique on natural, unprepared surfaces. These samples are a subset of the Leighty [1997] samples examined in the spectroscopic study of Feely and Christensen [1999; see also Hamilton, 1998]. The natural surfaces of several of these samples do not exhibit obvious signs of weathering (e.g., desert varnish or powdery material), but three samples exhibit clear evidence of surface weathering in the form of dusty surface coatings [Feely, 1997].

Mineral spectra from the Arizona State University (ASU) spectral library [Christensen *et al.*, this issue (b)] were used in the linear deconvolution (described below). These minerals are pure particulate samples having particle sizes from 710 to 1000 μm . This size fraction is optimized to minimize multiple scattering effects present in samples with small (0–75 μm) particle sizes and is a valid size fraction for comparison to solid samples (see discussion in section 3). These samples were

handpicked to remove visible impurities. Spectra from this library are available for online examination and download at <http://tes.la.asu.edu/> [Christensen *et al.*, this issue (b)].

2.2. Analysis Techniques

2.2.1. Thermal emission spectroscopy. Thermal infrared (2000–400 cm^{-1}) emission spectra of all samples were collected using the Mattson Cygnus 100 spectrometer at the ASU Thermal Emission Spectrometer Laboratory. Specific details regarding the spectrometer, sample environment, and data calibration techniques are discussed by Christensen and Harrison [1993] and Ruff *et al.* [1997]. Spectra of the rocks with cut surfaces (STL- and WAR-) are the average of two runs each of 180 scans, acquired over a period of approximately 5 min. Spectra of natural rock surfaces (RSL-) were collected by Feely [1997] using the average of 2–3 runs each of 260 scans. Each run in the natural surface average represents a different surface. Spectra were acquired such that a spot size of between 4 and 5 cm was observed; multiple runs were averaged, and this spot size was used to reduce preferential mineral observations due to heterogeneities in coarse-grained samples. Pure mineral spectra are from the ASU spectral library and were acquired according to the method detailed by Christensen *et al.* [this issue (b)].

2.2.2. Optical examination. Optical determinations of modal mineral abundances were carried out by one of the authors (V.E.H.) for all samples except those of the natural surface (RSL) suite, for which the modes were determined by Leighty [1997]. Errors in modal determinations are estimated at ± 10 –15 vol % for minerals with modes ≥ 10 and ± 5 vol % for minerals with modes < 10 vol % [see Leighty, 1997].

Although optical modes are nontraditional and somewhat difficult to obtain with certainty for volcanic rocks (owing to their fine-grained nature and possible presence of glassy components), it is important to obtain them for comparison to linear deconvolution results, which are in the form of modal abundances. Furthermore, because linear deconvolution is a primary tool for the analysis of remotely acquired spectra [e.g., Christensen *et al.*, this issue (a)] (a case in which bulk analysis is not possible), modal mineralogy becomes the basis for classification of spectrally measured rocks. For this reason, current studies by Wyatt *et al.* [1999] are examining new methods of classifying volcanic rocks on the basis of modal mineralogy. Although agreement of model-derived modes and optical modes would seem to support the accuracy of both methods to within the stated error, independent confirmation of optical modes may be obtained by comparison to normative mineralogy derived from bulk analysis. Although normative mineralogy is based on complete equilibrium crystallization and may not exactly represent the volumetric proportions in the mode, it at least provides a basis for comparison, and indicates that the optical modes are reasonable (Figure 1) [McBirney, 1993]. The most accurate verification might be obtained through use of a microprobe-based mapping technique, such as Feature Scan [Taylor *et al.*, 1996; Wyatt *et al.*, 1999]; however, this type of analysis is very time consuming, approximately 1–2 days per sample, and it was not practical to analyze all of the samples in this study using this technique.

2.2.3. Electron microprobe. Leighty [1997] collected electron microprobe analyses for mafic minerals in a few rocks from the natural surface analysis group. One of the authors (V.E.H.) obtained chemistries for all major minerals (plagioclase, orthopyroxene and clinopyroxene) of the cut rocks from

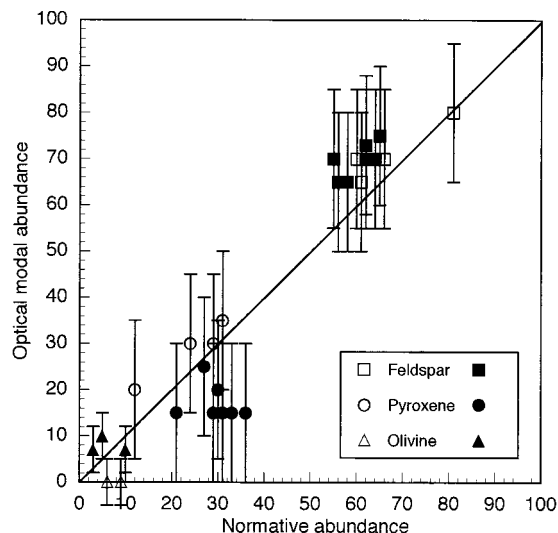


Figure 1. Optical modes versus normative mineralogy for representative rocks in this study. Norms were calculated from bulk chemistry in Table 2. Error bars are the maximums stated for the optical modes. The open symbols are STL samples, and the solid symbols represent RSL samples. Some plot points represent more than one measurement.

the Stillwater Complex on a JEOL JXA-8600 Superprobe operated and maintained by the Department of Chemistry at ASU. The error associated with the total of any individual microprobe analysis is $\pm 2\%$ (S. M. Peacock, personal communication, 1997); any analyses summing to less than 98.00% or greater than 102.00% were discarded.

2.2.4. Bulk analysis. Leighty [1997] provides bulk chemistries for samples in the natural surface analysis group. Bulk analysis of all other samples was obtained via standard induction coupled plasma mass spectroscopy (ICP MS), performed at an external laboratory, Bondar-Clegg, Inc., of Vancouver, British Columbia, Canada. Weight percent oxides for each sample are shown in Table 2.

3. Linear Deconvolution

The technique applied in this work is the same as that described by Hamilton *et al.* [1997], using the method of Ramsey and Christensen [1998], as implemented by J. Bandfield (personal communication, 1998). Input parameters to the deconvolution algorithm include a collection of pure mineral spectra (end-members), spectra of the rocks to be deconvolved, and a wavelength range over which the rock spectra are modeled. Outputs are a best fit model spectrum, modal percentages of end-member minerals used in the best fit spectrum, and a residual error spectrum, which is the difference between the measured and modeled spectrum at each wavelength. Also provided is the root-mean-square (RMS) error for each iteration. The RMS error is best used as an indicator of the goodness of fit for a particular iteration of the model for a given sample, whereas the residual error spectrum is best used as an indicator of the accuracy of the final model spectrum relative to the measured spectrum. In the absence of atmospheric components or wavelength-dependent variations in signal to noise ratio (SNR), such as in these laboratory data, wavelength regions with particularly high residual error are most likely to be

Table 2. Rock Sample Bulk Chemistry

Sample	SiO ₂	TiO ₂	Al ₂ O ₃	FeO ^(T)	MgO	CaO	Na ₂ O	K ₂ O	LOI	Total
RSL-11-94-2	51.20	1.13	16.90	8.54	6.30	9.93	3.00	1.05	N/A	98.50
RSL-12-94-8	53.90	1.00	16.20	8.00	5.60	8.72	3.40	1.31	N/A	98.60
RSL-4-95-23	50.80	1.56	14.80	9.92	7.00	10.32	3.00	0.96	N/A	98.90
RSL-9-94-12	55.00	1.27	15.20	8.31	7.30	7.66	3.30	1.22	N/A	99.60
RSL-9-94-36	53.10	1.57	15.00	10.30	7.90	8.77	3.10	0.60	N/A	100.80
RSL-9-94-41	50.80	0.94	17.50	8.72	7.10	9.75	3.30	0.89	N/A	99.50
RSL-9-94-42	52.60	1.11	17.50	8.01	5.70	9.30	3.50	1.10	N/A	99.40
STL-5	49.06	0.15	19.69	3.94	7.69	16.23	1.96	0.06	0.59	99.37
STL-20	49.32	0.10	25.74	3.08	4.53	13.45	2.59	0.09	0.59	99.49
STL-50	51.47	0.17	18.97	5.62	7.20	12.43	2.81	0.13	0.59	99.39
STL-100	49.11	0.06	21.99	3.28	9.23	14.47	1.61	0.03	0.44	100.22
STL-138	48.84	0.08	20.03	3.53	9.27	15.44	1.54	0.03	0.79	99.55
WAR-R0039	41.97	2.21	12.68	10.96	12.25	12.90	1.76	0.76	3.72	99.20
WAR-R0519	53.59	0.88	18.46	7.42	5.41	8.82	3.88	0.60	0.05	99.11
WAR-R1049	49.54	2.05	12.67	13.15	6.15	9.13	2.76	0.43	2.32	98.20
WAR-R1079	42.23	0.51	9.69	7.83	20.67	9.72	1.67	1.13	4.74	98.19
WAR-R2624	52.45	1.11	14.80	10.12	5.85	9.66	3.13	0.79	0.73	98.64
WAR-R3309	47.58	2.24	15.82	12.58	7.11	8.67	3.22	0.91	0.03	98.16
WAR-R3319	51.82	0.89	18.55	5.71	5.13	10.68	3.82	0.68	1.98	99.26
WAR-R6479	54.05	0.12	3.50	9.29	28.10	2.79	0.45	0.06	0.15	98.51

Values are in units of wt % oxide. All Fe is reported as FeO^(T). LOI, loss on ignition.

indicative of spectral components that are not adequately modeled [Ramsey and Christensen, 1998].

The accuracy with which the modal mineralogy of a rock may be determined from its spectrum is dependent on a variety of factors, including characteristics of the physical sample, the end-member minerals, and the spectral data. As the abundance of a given mineral in the physical sample increases, it is more likely to be detected because its spectral features become distinguishable from noise in the data and provide an increasingly greater contribution to the bulk spectrum. Ramsey and Christensen [1998] examined two-mineral physical mixtures of calcite and quartz (minerals with strong spectral features that do not overlap). They observed that for cases in which a mineral was present at 5 vol % or less, the modeled abundance was much less accurate than in cases in which both minerals had abundances >5 vol % (errors ranged from 2 to 75% of the actual mode; absolute errors Δ of up to 3.75 vol %). The Ramsey and Christensen test was a best case example, with only two minerals in the mixture and two mineral end-members. Therefore results for multiminerale mixtures of silicates using a large number of end-members are expected to have errors at least equivalent to the Ramsey and Christensen result and probably, in practice, somewhat greater. There are small (0.5% daily to 4% over time) contributions to error in the measured spectra as a result of instrument noise and instrument precision [Ramsey and Christensen, 1998]. Therefore modal determinations <5–7 vol % in the model fit should be carefully considered. An additional impact on accuracy comes from the available end-member minerals. Even with a compositionally broad library of end-member minerals, it is highly unlikely that any mineral in the library (e.g., olivine) will have the exact same chemistry as the mineral in a rock because most rock-forming minerals exhibit natural variability due to solid solution. The resulting model modes reflect this difference, and these effects are discussed in section 4.2. Finally, characteristics of the spectral data, such as spectral resolution and noise, also impact the model accuracy. The effect of decreased spectral resolution is discussed in section 6.

The algorithm was run twice for each sample to provide the best constraints on modal mineralogy. First, each rock spec-

trum was deconvolved using the full ASU spectral library (over 150 end-members). For samples with cut surfaces, between 70 and ~100 vol % of the modal mineralogy was modeled by the primary minerals feldspar, pyroxene, and/or olivine and the secondary mineral serpentine; most other minerals were determined to be present only in small abundances (<10 vol %) that are near or below the known detectability limits of the technique (~5–7 vol %) [Ramsey and Christensen, 1998]. For the samples with natural surfaces, similar results were obtained but with slightly increased quantities of alteration minerals such as clays and serpentines. Although the model fit becomes better with increasing numbers of end-members, such fits are difficult to interpret because small amounts of many end-members may be used to fit minor deviations between the model and the measured spectra. To better constrain the geologically significant modes, we assume that these rocks can be modeled by limiting the end-member set to the minerals that were most abundant in the first iteration, in this case, representing minerals commonly found in mafic igneous rocks. The second deconvolution run used such a subset, including alkali and plagioclase feldspars, orthopyroxenes and clinopyroxenes, and olivines. Amphiboles, serpentines, and micas were included because they are common alteration products of the primary minerals. Although rare in these types of rocks, quartz and carbonate were also added. Clays were added to the end-member set used for the deconvolution of natural surfaces. The end-member minerals used for the second (final) deconvolution are listed in Table 3 along with their compositions as determined by electron microprobe or bulk (e.g., feldspars) analysis.

Minerals generally considered accessories in these types of rocks, such as opaques, were not included, nor were glass spectra. The only glass spectra available at the time of this study represent obsidian glasses, which are not necessarily representative of glassy phases in basaltic extrusive samples (see Wyatt *et al.* [1999] for high-quality modes and glass analyses of spectrally analyzed basaltic and andesitic rocks). Because glass phases were not generally identified in the optical modes, we opted to omit this end-member. Ongoing studies by Wyatt *et al.* [1999] are examining the spectra of basaltic glasses and will

Table 3. End-Member Bulk Compositions

Sample	SiO ₂	TiO ₂	Al ₂ O ₃	FeO ^(T)	MnO	MgO	CaO	Na ₂ O	K ₂ O	P ₂ O ₅	Cr ₂ O ₃	Total
Plutonic quartz	100.00	0.00	0.00	0.00	0.00	0.00	0.00	0.00	0.00	0.00	0.00	100.00
Vein quartz	100.00	0.00	0.00	0.00	0.00	0.00	0.00	0.00	0.00	0.00	0.00	100.00
Microcline AK-01	63.89	0.01	16.90	3.43	0.02	0.14	0.07	0.18	14.50	0.01	0.03	99.18
Microcline BUR-3460	63.45	0.01	19.12	0.13	0.01	0.01	0.16	2.77	12.03	0.56	0.01	98.26
Microcline BUR-3460A	64.22	0.01	19.05	0.17	0.01	0.01	0.02	3.12	12.97	0.05	0.01	99.64
Microcline WAR-5918	64.05	0.01	18.41	1.02	0.01	0.12	0.27	2.64	10.93	0.01	0.09	97.56
Microcline WAR-0650	59.88	0.02	18.41	5.48	0.03	0.43	0.32	1.35	11.25	0.01	0.61	97.79
Orthoclase WAR-5919	62.19	0.01	19.09	1.71	0.01	0.08	0.72	2.50	10.17	0.01	0.18	96.67
Sanidine WAR-RGSAN01	63.05	0.04	19.05	3.78	0.02	0.24	0.56	1.94	10.72	0.01	0.40	99.81
Anorthoclase WAR-0579	61.12	0.15	19.35	3.01	0.04	0.98	2.57	5.61	4.20	0.06	0.19	97.28
Perthite WAR-5802	66.33	0.01	18.33	1.44	0.01	0.24	0.44	5.07	7.09	0.01	0.12	99.09
Albite WAR-0235	68.30	0.03	19.98	0.37	0.01	0.04	0.01	11.54	0.02	0.03	0.02	100.35
Albite WAR-0244	69.16	0.01	18.18	0.27	0.01	0.01	0.38	10.20	0.66	0.38	0.02	99.28
Albite WAR-0612	66.43	0.02	18.79	1.29	0.02	0.40	0.35	9.15	0.18	0.16	0.12	96.91
Albite WAR-5851	63.03	0.01	19.67	5.51	0.02	0.47	1.37	8.50	0.22	0.01	0.63	99.44
Oligoclase WAR-5804	60.08	0.01	22.29	0.17	0.01	0.01	4.01	8.48	0.71	0.06	0.01	95.84
Oligoclase (perist.) BUR-060	60.41	0.01	21.88	4.16	0.08	0.06	3.24	9.37	0.79	0.01	0.10	100.11
Oligoclase (perist.) BUR-060D	63.49	0.01	22.50	0.21	0.01	0.01	3.36	9.21	0.60	0.05	0.01	99.46
Oligoclase (perist.) WAR-RGOL101	61.57	0.01	22.82	1.05	0.01	0.32	3.36	7.33	0.67	0.01	0.10	97.25
Oligoclase WAR-0234	60.06	0.02	21.78	1.31	0.02	0.84	5.31	6.63	0.90	0.01	0.10	96.98
Andesine WAR-0024	53.49	0.66	23.32	5.69	0.07	2.38	8.90	4.43	0.72	0.05	0.12	99.83
Andesine BUR-240	53.85	0.12	27.09	0.59	0.01	0.07	9.51	5.55	0.37	0.10	0.02	97.28
Labradorite WAR-4524	52.62	0.11	27.74	2.50	0.02	0.14	10.90	5.01	0.42	0.03	0.04	99.53
Labradorite BUR-3080A	53.38	0.44	26.25	1.67	0.03	0.65	9.62	4.94	1.20	0.12	0.08	98.38
Labradorite WAR-RGAND01	49.85	0.05	28.03	3.09	0.03	0.68	13.04	3.46	0.22	0.01	0.22	98.68
Labradorite ASU Mineral Lab	52.62	0.11	27.74	2.50	0.02	0.14	10.90	5.01	0.42	0.03	0.04	99.53
Labradorite WAR-5877	52.32	0.07	28.84	1.56	0.01	0.31	12.55	3.93	0.40	0.01	0.12	100.12
Bytownite WAR-5859	48.35	0.04	31.54	1.56	0.01	0.26	14.68	2.89	0.09	0.01	0.12	99.55
Bytownite WAR-1384	49.91	0.08	30.07	2.97	0.03	0.49	11.47	3.54	0.25	0.01	0.25	99.07
Anorthite BUR-340	44.84	0.01	35.01	0.37	0.00	0.00	18.25	0.94	0.00	0.00	0.00	99.42
Anorthite WAR-5759	41.54	0.03	29.50	9.20	0.03	2.69	15.40	1.13	0.08	0.01	0.98	100.59
Hornblende WAR-0404	42.69	0.90	14.56	12.80	0.10	13.46	9.83	2.75	0.94	0.07	0.10	98.20
Hornblende HS-177.4b	42.93	2.27	11.38	15.45	0.11	11.21	12.05	2.12	1.53	0.11	0.12	99.28
Magnesio-hornblende HS-115.4b	45.12	0.24	9.94	8.31	0.09	18.69	11.73	2.20	0.78	0.01	0.16	97.27
Richterite ASU-03	54.13	0.33	2.31	3.55	0.15	22.15	8.74	4.42	1.39	0.01	0.10	97.28
Katophorite BUR-2660	45.33	0.87	5.86	20.49	1.12	10.14	5.82	5.12	1.29	0.07	0.10	96.21
Amphibole BUR-1700	43.65	0.52	8.50	31.58	0.49	6.37	1.22	0.65	2.01	0.37	0.11	95.47
Amphibole WAR-0219	47.90	1.20	13.22	13.28	0.24	7.87	8.52	3.70	0.03	0.08	0.19	96.23
Anthophyllite BUR-4760	60.08	0.10	0.84	2.63	0.43	27.32	3.50	0.90	0.17	0.01	0.07	96.05
Actinolite HS-116.4b	54.72	0.06	1.53	6.96	0.16	21.33	11.13	1.03	0.08	0.12	0.22	97.34
Actinolite WAR-0354	54.00	0.04	2.07	6.89	0.23	20.03	11.48	0.99	0.06	0.01	0.28	96.08
Tremolite HS-315.4b	53.38	0.22	2.29	3.94	0.29	22.26	11.46	0.86	0.39	0.01	0.12	95.22
Biotite edges	39.03	2.17	11.20	19.67	0.80	13.99	0.51	0.53	8.80	0.01	0.01	96.72
Biotite face	39.03	2.17	11.20	19.67	0.80	13.99	0.51	0.53	8.80	0.01	0.01	96.72
Muscovite WAR-5474	48.60	0.45	29.40	5.80	0.28	0.52	0.03	9.87	0.40	0.03	0.00	95.38
Phlogopite HS-23.3b	40.29	1.24	13.77	1.87	0.01	25.85	0.01	0.25	9.74	0.00	0.00	93.03
Chlorite BUR-1340	28.73	0.47	17.48	8.03	0.15	30.95	0.01	0.01	0.01	0.03	0.17	86.04
Clinoclase WAR-1924	32.00	0.01	16.00	3.76	0.01	33.90	0.09	0.07	0.07	0.03	0.00	85.94
Kaolinite (solid)	45.10	1.66	39.20	0.21	0.00	0.06	0.03	0.03	0.02	0.00	0.00	86.31
Dickite (powder)	45.10	1.66	39.20	0.21	0.00	0.06	0.03	0.03	0.02	0.00	0.00	86.31
Illite (granular)	55.10	0.63	22.00	6.00	0.00	2.80	0.02	0.08	8.04	0.00	0.00	94.67
Enstatite NMNH-34669	57.03	0.00	0.39	6.36	0.15	35.46	0.11	0.01	0.00	0.00	0.00	99.50
Enstatite HS-9.4b	57.87	0.02	0.99	6.87	0.17	34.86	0.67	0.00	0.00	0.00	0.00	101.45
Enstatite NMNH-38833	56.39	0.02	1.08	6.89	0.15	33.83	0.30	0.00	0.00	0.00	0.00	98.67
Enstatite DSM-ENS01	58.57	0.01	0.27	6.47	0.17	34.44	0.20	0.00	0.00	0.00	0.00	100.12
Enstatite NMNH-82436	55.93	0.01	1.12	6.72	0.13	31.40	4.16	0.04	0.00	0.00	0.00	99.51
Enstatite NMNH-R14440	57.25	0.02	0.33	6.21	0.12	35.21	0.32	0.01	0.00	0.00	0.00	99.47
Bronzite NMNH-C2368	51.88	0.32	4.24	15.15	0.25	25.34	2.05	0.03	0.01	0.00	0.00	99.26
Bronzite BUR-1920	54.45	0.15	0.97	13.76	0.28	27.88	0.77	0.01	0.00	0.00	0.00	98.27
Bronzite NMNH-93527	51.84	0.35	5.28	13.78	0.23	26.76	1.46	0.07	0.00	0.00	0.00	99.79
Bronzite NMNH-166555	49.33	0.04	15.89	14.08	0.20	17.54	7.33	0.18	0.00	0.00	0.00	104.59
Bronzite NMNH-119793	55.66	0.11	2.27	8.08	0.17	32.29	1.03	0.02	0.00	0.00	0.00	99.62
Hypersthene NMNH-B18427	51.17	0.51	3.78	19.26	0.30	22.16	2.24	0.13	0.01	0.00	0.00	99.57
Diopside NMNH-107497	54.99	0.01	0.31	0.85	0.02	18.17	25.40	0.10	0.00	0.00	0.00	99.84
Diopside HS-15.4b	54.60	0.01	0.47	2.53	0.19	16.23	25.35	0.45	0.00	0.00	0.00	99.83
Diopside WAR-5780	54.14	0.02	0.51	2.56	0.06	17.54	24.25	0.45	0.00	0.00	0.00	99.53
Diopside BUR-1820	54.30	0.05	0.31	2.67	0.13	16.68	25.29	0.23	0.00	0.00	0.00	99.65
Diopside NMNH-80819	53.66	0.05	0.88	3.24	0.15	16.57	24.97	0.13	0.00	0.00	0.00	99.65
Diopside NMNH-R15161	54.06	0.03	0.71	3.96	0.17	15.86	24.75	0.37	0.00	0.00	0.00	99.91
Diopside NMNH-R17421	53.31	0.01	0.32	7.02	0.46	13.70	24.70	0.06	0.00	0.00	0.00	99.59
Diopside NMNH-119197	53.32	0.02	0.78	5.96	0.58	14.42	23.49	0.46	0.00	0.00	0.00	99.03
Diopside HS-119.4b	52.87	0.02	0.92	10.20	0.29	11.91	24.08	0.65	0.00	0.00	0.00	100.95
Augite WAR-6474	50.60	0.18	2.35	12.58	0.30	9.96	21.13	2.00	0.00	0.00	0.00	99.10

Table 3. (continued)

Sample	SiO ₂	TiO ₂	Al ₂ O ₃	FeO ^(T)	MnO	MgO	CaO	Na ₂ O	K ₂ O	P ₂ O ₅	Cr ₂ O ₃	Total
Augite NMNH-9780	51.00	0.20	1.55	16.52	0.46	9.42	20.49	0.33	0.02	0.00	0.00	99.99
Augite BUR-620	50.51	0.11	1.69	16.19	0.73	7.58	21.51	1.91	0.00	0.00	0.00	100.23
Augite WAR-5858	50.58	0.79	3.23	7.13	0.16	16.82	19.81	0.36	0.01	0.00	0.00	98.87
Hedenbergite DSM-HED01	49.96	0.01	0.06	14.14	7.99	4.32	22.80	0.11	0.00	0.00	0.00	99.39
Hedenbergite NMNH-R11524	48.06	0.01	0.23	23.82	3.27	1.06	22.85	0.06	0.00	0.00	0.00	99.35
Serpentine HS-8.4b	42.28	0.01	1.21	3.79	0.06	38.50	0.02	0.01	0.01	0.00	0.00	85.89
Serpentine BUR-1690	38.70	0.02	1.15	8.81	0.15	39.11	0.04	0.01	0.01	0.01	0.00	88.01
Lizardite 83-145B	40.49	0.01	1.18	6.30	0.11	38.81	0.03	0.01	0.01	0.01	0.00	86.96
Forsterite BUR-3720A	41.95	0.01	0.49	8.49	0.13	49.33	0.38	0.02	0.12	0.00	0.00	100.92
Forsterite AZ-01	38.47	0.01	0.09	9.57	0.13	48.88	0.14	0.03	0.01	0.01	0.00	97.34
Fayalite WAR-RGFAY01	31.11	0.06	0.00	59.75	1.30	7.71	0.09	0.00	0.00	0.00	0.00	100.02
Calcite C27	0.00	0.00	0.00	0.00	0.00	0.26	56.48	0.00	0.00	0.00	0.00	56.74
Dolomite C20	0.00	0.00	0.00	0.00	0.07	19.71	30.01	0.00	0.00	0.00	0.00	49.79

Values are in units of wt % oxide. All Fe reported as FeO^(T).

permit the reanalysis of these samples once better end-member spectra and modal analyses are available. The exclusion of mineral end-members representing minor components automatically induces some amount of misfit in the model of any sample known to contain one of these minerals. Because the deconvolution algorithm calculates fractional percentages which sum to 100 vol % (see Ramsey and Christensen [1998] for details), this misfit will be expressed in the model results as a redistribution of the percentage of the mineral not modeled. For example, if 4 vol % chromite is present in the rock but cannot be modeled because the appropriate end-member is not available, some or all of the minerals included in the final fit will have slightly inflated modal abundances.

A portion of the spectral signature of water vapor at high wavenumbers (short wavelengths) very broadly mimics an absorption feature in carbonates and is commonly incorrectly modeled as carbonate when this region of the spectrum is included in the deconvolution. To eliminate this effect and prevent a degradation of the fit over the rest of the spectrum, the wavelength range of the deconvolution was set from 1250 to 400 cm⁻¹, which excludes the region of water vapor absorptions but still includes all silicate features. Carbonate, if present, exhibits sharp absorption bands within this region that would allow its discrimination, even at relatively small (5 vol %) modal abundances.

Two issues arise relating to spectral contrast and particle size in the rock and pure mineral spectra. The first is the observation that pure mineral spectra commonly display greater spectral contrast than the rocks in which they occur. In order to account for such differences in spectral band depth between the rock and the end-members, Hamilton *et al.* [1997] included a blackbody end-member (unit emissivity at all wavelengths) in the end-member suite. The same approach has been followed in this study. When included in a model fit, a blackbody reduces the spectral contrast uniformly across the spectrum but does not change spectral shapes or band positions. The presence of the blackbody end-member in a model fit acts to mathematically reduce or eliminate differences in spectral band depth between the end-member mineral spectra and the rock spectrum.

The second issue is the use of spectra of particulate mineral samples to model bulk rock spectra. Coarse (710–1000 μm) particulate minerals are used in the Christensen *et al.* [this issue (b)] spectral library because they can be handpicked to reduce contaminants and because it is commonly difficult to obtain large crystals of pure minerals. However, it has been observed

that decreasing the mean particle size of a sample, at particle sizes greater than about 65 μm, results in a uniform decrease in spectral contrast, with no change in the positions of the primary absorptions [Lyon, 1965; Hunt and Vincent, 1968; Salisbury and Wald, 1992; Moersch and Christensen, 1995]. This decrease is attributed to the pore spaces between the grains acting as blackbody cavities, reducing the spectral contrast of the sample by adding some fixed amount of unit emissivity to the spectrum [Salisbury and Eastes, 1985]. Thus it is possible that the spectral signature of a given rock (which has no pore spaces and virtually no change in *n* at grain boundaries) may have deeper features than the particulate equivalent of that rock. Hamilton [1999a] demonstrated that the difference in spectral contrast between the spectrum of a basaltic rock and the spectrum of that rock crushed to particulate sizes of 710–1000 μm was ~67%, or roughly the equivalent of adding 33% blackbody to the rock spectrum. This percentage appears to vary slightly with rock type. A similar study of a granitic rock [Ruff, 1998] exhibited a decrease of ~40% in the particulate sample. In order to ensure that the spectra of the rocks were approximately equivalent to the spectra of the particulates that would be used in the model, 35% blackbody (an intermediate value weighted toward the percentage observed for the basaltic sample) was added to all rock spectra prior to deconvolution. (Rock samples could be crushed prior to analysis, but this would require additional preparation time and is not possible in remote sensing situations, whereas addition of blackbody to the spectra only takes a few seconds.) The effect of this addition may be to increase the use of the blackbody end-member in the model fits, particularly in the event that a rock spectrum already exhibited less spectral contrast than the component mineral spectra. However, this should not have a negative impact on model results because there are no changes to the spectral shapes or band positions due to the addition of blackbody.

4. Results and Discussion

Overall, the spectral fits produced by the linear deconvolution algorithm are extremely good. Feely and Christensen [1999] also analyzed the natural surface spectra shown in this study. Model results from these two studies are not identical due to slight differences in the application of the deconvolution and the end-member suites; however, despite these differences, the results are quite similar. Rock and model spectra for all samples are shown in Figures 2–4. The best model fit of all 20

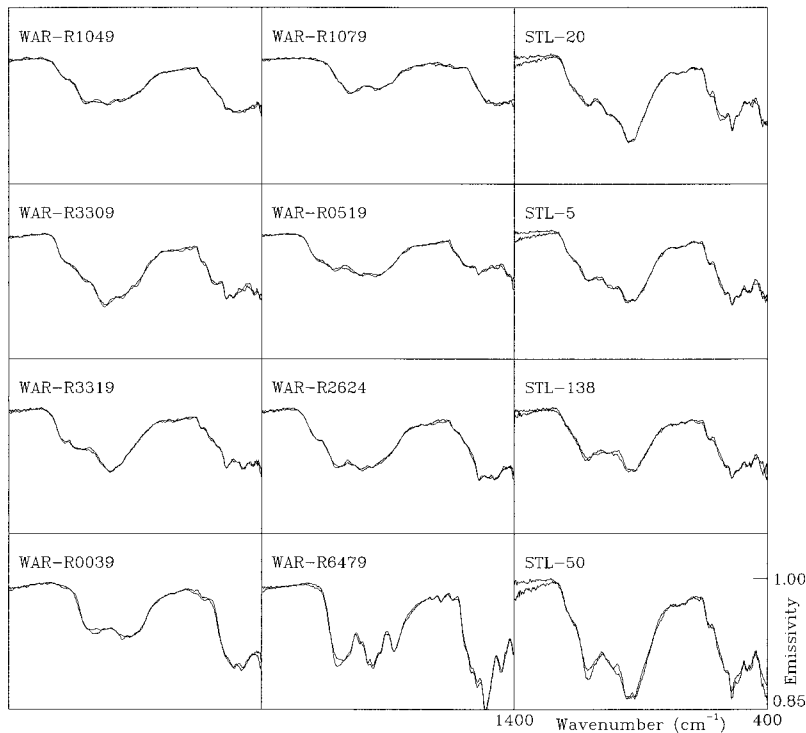


Figure 2. Measured and modeled emissivity spectra for rocks with cut surfaces. Spectra are shown at full spectral contrast, without blackbody components.

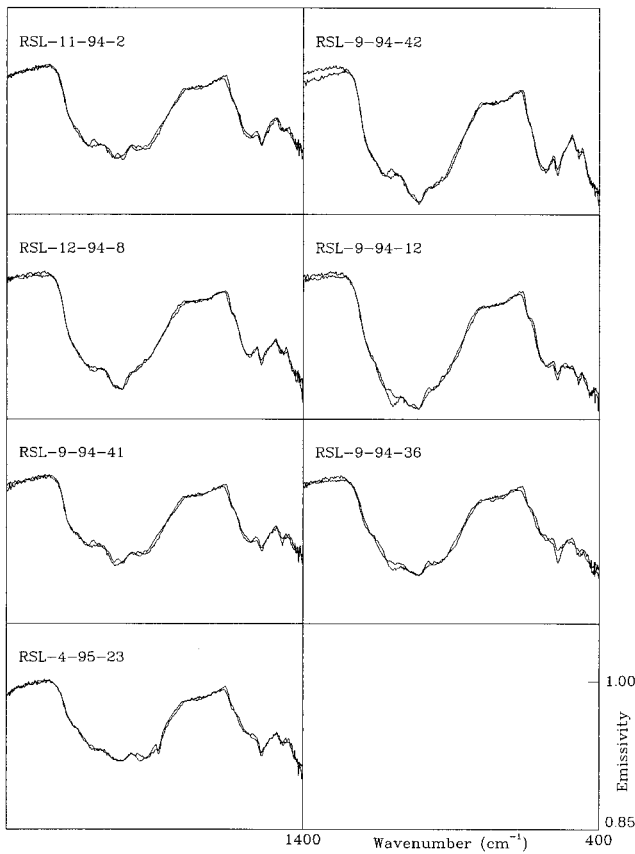


Figure 3. Measured and modeled emissivity spectra for rocks with natural surfaces. Spectra are shown at full spectral contrast, without blackbody components.

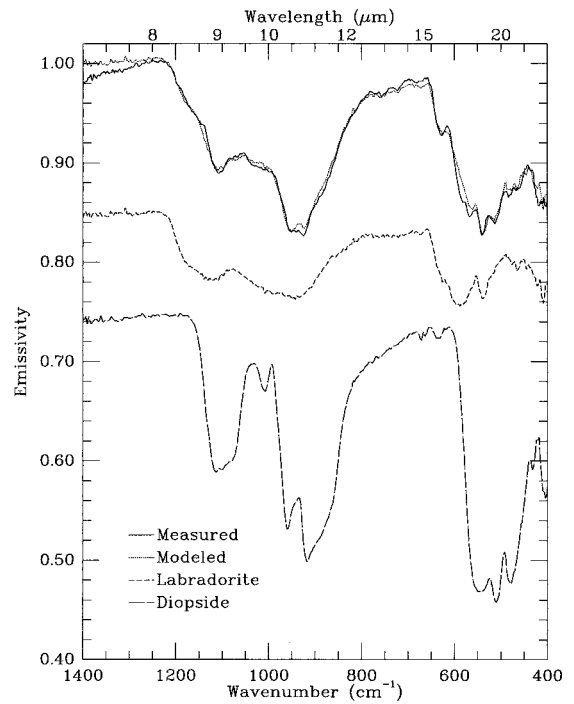


Figure 4. Measured and best fit spectra for sample STL-100, with the two primary library end-members used in the best fit spectrum. Labradorite sample is WAR-RGAND01, and diopside sample is NMNH-107497. Mineral spectra are offset for clarity. Spectra are shown at full spectral contrast, without blackbody components.

Table 4. Deconvolution Results for STL-100

End-Member	Modeled vol %	Normalized vol %	Mineral Group	Group Mode, vol %	Optical Mode, vol %
Albite WAR-5851	1	1			
Labradorite WAR-RGAND01	36	43			
Anorthite BUR-340	3	4			
Anorthite WAR-5759	18	21	feldspar	68	70
Diopside NMNH-107497	13	15	clinopyroxene	15	15
Bronzite NMNH-166555	10	12			
Hypersthene NMNH-B18427	2	3	orthopyroxene	15	15
Forsterite AZ-01	3	3	olivine	3	N/A
Blackbody	16	[0]			
Total	101	101		101	100

Total modes >100 vol % are the result of rounding errors. N/A, not available.

samples was for cut surface sample STL-100 (Figure 4). STL-100 contained three major minerals, all of which were modeled to within 2 vol % of the optically determined mode (Table 4). The average difference between the optically measured and modeled modes for feldspar, pyroxene, and olivine in all 20 rocks is only 5 vol % (standard deviation of 5). The biggest differences between the optically derived and modeled modes were observed for cut sample WAR-R3319, which exhibited errors of up to 30 vol %, despite a very high-quality, low-RMS spectral fit (see Figure 2). The goodness of the spectral fit suggests that the problem was not due to incorrect end-members in the model; it is more likely that this error is attributable to (1) heterogeneity in the rock (observable in hand sample), such that the thin section material was not representative of the surface that was analyzed spectrally, or (2) alteration at submicroscopic scales (discussed below). Virtually no errors were found to occur systematically across the cut and natural surface groups. Among samples containing olivine, the modal abundance modeled typically fell below that observed optically; however, measured olivine modes were generally less than 10 vol %, thus approaching the limits of the algorithm's accuracy.

The deconvolution results for all samples included the blackbody end-member in amounts ranging from 14 to 65% of the total mode with an average of 33% (standard deviation of 12). This result indicates that in all cases, the spectra produced by the model end-members had greater spectral contrast than the rock spectra. The average value of 33% is very close to the amount of blackbody (35%) that was added to the rock spectra in order to mimic the spectral contrast of a particulate rock. This suggests that the addition of blackbody to the rock spectra may have been unnecessary, at least in cases where the spectral contrast of a bulk rock was equivalent to or less than that of the end-member mineral spectra used in the best fit. However, for cases in which the bulk rock spectra had deeper spectral features than the mineral end-member spectra used in the best fit, this blackbody addition was necessary because there is no way to artificially deepen spectral features in the model fit. Feely [1997] found that in such cases, end-member minerals with the greatest spectral contrasts were overestimated to mathematically reduce the difference between the measured and modeled spectrum. Because there is no way to tell in advance whether a rock spectrum has greater spectral contrast than the end-members that will be used in the best fit of the deconvolution, it is suggested that this procedure be applied to all bulk rock samples. This has the added benefit of ensuring that all

samples are analyzed in the same manner. Even if the blackbody is unnecessary in some samples, subsequent removal of the blackbody mode and normalization of the mineral modes to 100% requires little effort.

The linear deconvolution results are discussed below in several sections describing different aspects and implications of the model fits for cut and natural surfaces. The first section examines the accuracy of the model in determining modal abundances of each mineral class. In the second section the accuracy of the model in approximating the correct solid solution composition using available end-members is discussed. Finally, the third section describes the comparison of measured bulk oxide data to oxides derived from the end-members used in the model fit.

4.1. Accuracy in Determination of Modal Abundances

4.1.1. Samples analyzed on cut surfaces. Figure 5 shows the comparison between the model-derived and optical modal abundances for the primary minerals found in the 13 rocks in

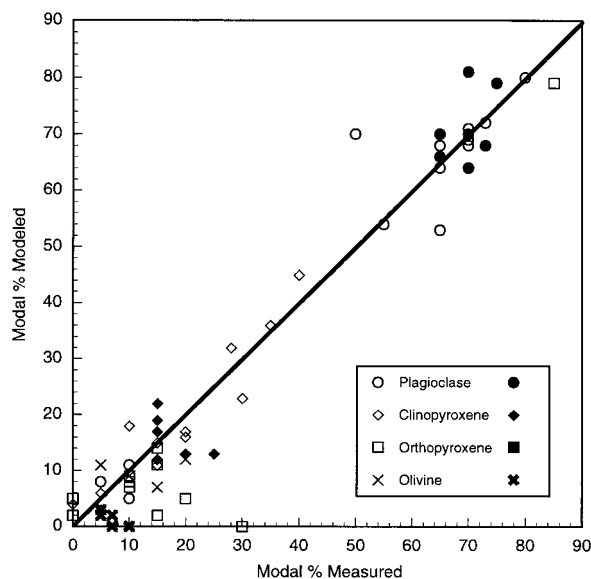


Figure 5. Comparison of optical and model-derived modes for major/primary minerals in all rock samples. Open symbols represent data for rocks analyzed on cut surfaces, and solid symbols represent data for rocks analyzed on natural surfaces. Some plot points represent more than one measurement.

this group. For the purpose of examining modal abundances of major/primary minerals, minerals of the same class in all of the final model results were grouped together. For example, if three different plagioclase end-members are included in a model fit at 12, 17, and 27 vol %, the total plagioclase mode is 56 vol %. Of a total of 41 measurements of primary minerals, only one mineral observed optically was not detected. Three minerals detected at ≤ 5 vol % were not observed optically; these may reflect heterogeneity of the samples with respect to the thin section, or model minimization of the residual error around minor spectral features. Both of these cases are likely, and similar results are not uncommon in many of the spectral fits. These errors are not of great concern because they are not geologically significant abundances (for primary minerals) and because modeled modes under 5 vol % are known to be less reliable, as described above. Thirty-eight minerals (93%) were modeled to within the error associated with the optical measurement (± 10 – 15 vol % for modes ≥ 10 vol %, ± 5 vol % for modes < 10 vol %). Of the 33 minerals observed optically at > 10 vol %, 29 (88%) were modeled to within 10 vol % of the optical mode. These results indicate that the model-derived modes correlate extremely well ($y = 0.992(x - 1.478)$, $R^2 = 0.923$) with the modes derived optically.

Two of the points that deviate significantly from the 1:1 best fit line in Figure 5, one plagioclase (measured:modeled 50:70) and one orthopyroxene (30:0), are both modes for sample WAR-R3319. In thin section this rock, a norite, was observed to contain significant amounts (15–20 vol %) of biotite and/or muscovite, which suggest that this rock has been altered since its crystallization. Although amphibole was not identified optically in significant abundances, ~ 20 vol % hornblende comprises the model fit. There are two possible reasons for this disagreement, and both may apply. First, as mentioned previously, the modeled spectrum provided a good fit to the rock spectrum, suggesting that the optical mode may not represent adequately the modal mineralogy of the surface that was measured spectrally. Second, the exact type of alteration experienced by this rock is unknown, and it is possible that there are chemical changes at submicroscopic scales that prevent accurate optical identification of the minerals comprising the rock. Under this hypothesis, the opx is undergoing a process of alteration, possibly at the silicate-chain scale [cf. *Sharp et al.*, 1996], of conversion from single-chain pyroxene to double-chain amphibole. Such a conversion might not be observable at petrographic microscope magnifications but could certainly affect the vibrational character of the energy emitted by the “orthopyroxene” grains. Thus orthopyroxene is not identified, and hornblende is. It follows that the overabundance of plagioclase in the model is accommodating the underestimation of the pyroxene phase (only ~ 20 vol % was modeled by hornblende).

In several samples, minerals atypical for the rock type (in a pristine state) were observed in thin section. These secondary minerals, generally serpentine, micas, and amphibole, are assumed to be the result of either hydrothermal or metamorphic alteration of the samples subsequent to their crystallization. They generally comprise between 2 and 15 vol % of the rock but may exceed 30 vol % (e.g., serpentine in some basalts). These constituents are included in the model modes as well. The accuracy of the model in measuring these phases is generally equivalent to that for primary minerals but is much less important to rock type identification than for the major minerals; regardless, the identification of minor or secondary min-

erals can provide important information regarding the history of a rock subsequent to its formation.

Accessory minerals such as opaques are not uncommon in these samples, typically occurring at abundances of 2–5 vol %. Because there are no oxides in the end-member suite (as discussed in section 3), the actual percentage of each oxide present must get redistributed among the end-members used in the final model fit. For this suite of rocks the effect of this omission is likely to be strongest in the model results for sample WAR-R0039, which is estimated to have 5–7 vol % opaques (more than any other cut sample) based on petrographic analysis.

Quartz, a mineral that is generally incompatible with the compositions studied here, was detected in several samples at only 2–3 vol % (small quartz modes in mafic rocks were also observed by *Feely* [1997]). These modes are well below the detection limit of the algorithm and are not geologically significant. In examining the spectra in which quartz was modeled, we observed that all shared a similar spectral feature, a shoulder or kink, on the short-wavelength side of the silicate stretching bands. This shoulder is located near the center of the doublet in the quartz fundamental at ~ 1160 cm^{-1} . This feature is likely due to feldspar in the sample but can be best fit with the addition of a small amount of quartz. This is an example of minor modes that can be eliminated based on model limitations and geological reasoning.

4.1.2. Samples analyzed on natural surfaces. A comparison of the optical modes and the model-derived modes for the seven natural surface samples is shown in Figure 5. Despite modeled mineralogies indicating “contamination” of four of the rock spectra by surficial clays (discussed below), virtually all of the 21 primary mineral measurements have model-derived modes within the error bounds of the optical measurements. Only two minerals (olivines observed optically at or below 10 vol %) were not detected. All minerals that were detected were observed in thin section (with the exception of clays). Nineteen of 21 (90%) measurements were modeled to within the error for the optical measurement. Of the 14 measurements ≥ 10 vol %, 13 (93%) lie within 10 vol % of the optical mode. Olivine abundances, which range from 5 to 10 vol % in thin section, tend to be underestimated but fall within the $\pm 5\%$ error of the optical measurement in three of five cases.

Dusty material was observed on the surfaces of several of these samples. Deconvolution results for four of the samples (RSL-4-95-23, RSL-9-94-36, RSL-9-94-41, and RSL-9-94-42) include between 6 and 13 vol % of one or more clay end-members. There is no reliable trend in the model results that would indicate that any single primary mineral is being replaced by the clay mode. In two of the four samples, feldspar is modeled at the optical mode; in one sample it is overestimated by 4 vol %, and in the fourth, it is underestimated by 6 vol %. In three of the samples, pyroxene is overestimated by 2–7 vol % and underestimated by 3 vol % in the fourth. Olivine is underestimated or not detected in all four cases, from 3–10 vol %. While olivine weathers easily and may logically be absent from the most weathered surfaces, we are not confident that we can link the identification of clay and the absence of olivine because of the small total modal abundances of olivine and the inherent detectability limits of the linear deconvolution technique.

One sample, RSL-4-95-23, was observed in thin section to contain approximately 5 vol % calcite. Despite the limitation placed on the algorithm to fit bands between 1400 and 400

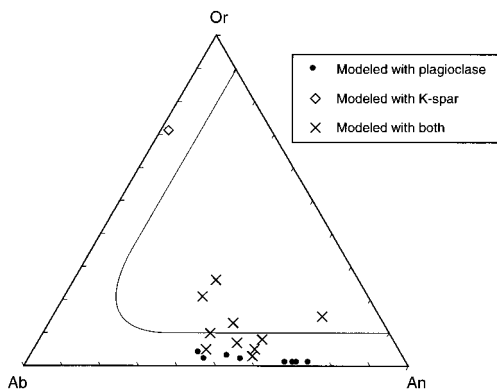


Figure 6. Modeled feldspar compositions for all 20 rocks. Dots represent samples modeled with plagioclase end-members only, the diamond represents a sample modeled with only alkali feldspar, and the crosses represent samples modeled with both plagioclase and alkali feldspar end-members. One plot point ($An_{68}Ab_{31}Or_1$) represents two samples.

cm^{-1} (which does not include the strongest calcite fundamental at $\sim 1525\text{ cm}^{-1}$), 8 vol % carbonate (half calcite, half dolomite) was detected due to the presence of a small, but sharp carbonate band at $\sim 880\text{ cm}^{-1}$ in the basalt spectrum.

4.2. Reproduction of Plagioclase and Pyroxene Solid Solution Compositions

In many cases, the model fit to a spectrum includes several end-members from within a solid solution series (e.g., plagioclase and pyroxene; see Table 4). Because it is probable that none of the spectral end-members represents exactly the same composition as a mineral in a given rock, it seems logical that multiple end-members may be used in the fit in order to reproduce the spectral contribution (i.e., composition) of a “real” mineral with a composition somewhere in between. *Hamilton et al.* [1997] demonstrated that forsteritic and fayalitic olivine spectra could be combined to produce the spectrum of an intermediate composition. This idea can be tested for feldspar and pyroxene in two ways. First, the compositions of the modeled end members of a mineral group (e.g., feldspars) can be combined in proportion to their relative abundances so that an assessment can be made of the “realness” of the chemistry; that is, whether or not the combined effective composition lies in a valid compositional space. Second, in cases where actual mineral chemistry is available, this model-derived effective composition can be compared to the actual composition of the mineral. All of the major minerals in each of the Stillwater (STL) samples have microprobe data available, as well as some of the mafic minerals in a few of the natural surface (RSL) samples [Leighty, 1997]. These data provide an excellent means of comparing the actual mineral compositions to the derived compositions in the model results.

4.2.1. Model-derived feldspar compositions: All rocks.

Feldspar compositions are defined by end-members anorthite ($An = CaAl_2Si_2O_8$), albite ($Ab = NaAlSi_3O_8$), and orthoclase ($Or = KAlSi_3O_8$). Compositions between the Na and K end-members are referred to as alkali feldspars, and minerals in the solid solution series between Na and Ca are called plagioclase. Feldspars in mafic and ultramafic lithologies are typically plagioclases having compositions with An numbers [$An/(An + Ab) \times 100$, ranging from 50 to 95+]. Naturally occurring plagioclases with An greater than ~ 30 are restricted to having

less than 10 vol % of the Or (potassium) component. Because alkali feldspars are less commonly found in ultramafic and mafic rocks, any modeled alkali feldspar will be combined with the modeled plagioclase to produce a weighted, average feldspar composition with the assumption that any Or component present is part of the plagioclase composition. The validity of this assumption will be discussed below. An example is provided from the modal results in Table 4. Four plagioclase feldspar end-members from the library were used in the best fit (an albite, a labradorite, and two anorthites). If we normalize these minerals’ modal abundances to 100%, then sum their known An, Ab, and Or compositions proportionally (determined from the data in Table 3), we obtain a single composition of $An_{74}Ab_{25}Or_1$.

The average compositions of the modeled feldspar compositions for all 20 rocks are shown in Figure 6. Nine of 20 compositions are modeled with plagioclase end-members only. Of the 11 samples modeled with some percentage of alkali feldspar, four have average compositions that fall outside the normal compositional space of feldspar. Therefore a total of 16 out of the 20 fall within the ternary regions of natural plagioclase compositions; of these 16, 15 have An numbers >45 , as expected for mafic and ultramafic lithologies (the 16th is comprised of alkali feldspar only). Additionally, even samples modeled with $>10\%$ Or component have An numbers >50 , indicating that the plagioclase component is generally correctly modeled.

As just described, four rock sample models have average feldspar compositions that are unrealistic for naturally occurring feldspars, and the modeled composition of another sample is pure alkali feldspar. The impact of these inaccuracies on the interpretation of model results will, in part, be strongly dependent not just on the total volumetric abundances of the modeled feldspar, but also the percentage of that feldspar that was modeled by potassium feldspar. For example, two of these five compositions ($An_2An_{27}Or_{72}$ and $An_70Ab_{15}Or_{15}$ in Figure 6) are correctly modeled at less than 12 vol % of the rocks they occur in; thus the contribution of these feldspars, while non-trivial, does not severely impact the spectral fit of the model (see WAR-R6479 and WAR-R1079 in Figure 2). In the other three samples, feldspar comprises 65–80 vol % of the rock. In sample RSL-9-94-36 ($An_{48}Ab_{39}Or_{13}$ in Figure 6), 70 vol % plagioclase was observed optically. The modeled amount was 64 vol %, of which only 2.5 vol % was indicated as K-spar (note that this 2.5 vol % is well below the ~ 5 vol % detectability limit). In this case, the addition of K-spar, while influencing the bulk composition slightly, does not result in any significant misfit in the modeled spectrum (Figure 2). The remaining two points ($An_{37}Ab_{37}Or_{26}$ and $Ab_{48}Ab_{39}Or_{13}$) are from samples in the natural surface suite, RSL-9-94-12 and RSL-9-94-36, respectively. The total feldspar abundance in both rocks was modeled to within 6 vol % of the optical mode, from ~ 65 to 70 vol %. In these samples, 23 and 25 vol % (respectively) was composed of potassium feldspar, with plagioclase components having average An numbers between 48 and 58 (reasonable for mafic rocks). However, in terms of absolute modal abundances, the high percentages (23 and 25 vol %) of modeled alkali feldspar are puzzling. If these rocks were more felsic, it might be possible to interpret average compositions falling outside the ternary compositional space as indicators that two feldspar phases, an alkali and a plagioclase, are present and that the assumption of a single feldspar phase is incorrect. However, because alkali feldspars are not commonly found in

Table 5. Comparison of Measured and Model-Derived Feldspar Compositions

Sample	Microprobe Composition/ Optical An Estimate	Modeled Plagioclase*	Modeled An Number
STL-5	An ₇₈ Ab ₂₂ Or ₀ (An ₇₈)	An ₆₈ Ab ₃₁ Or ₁	68
STL-20	An ₇₃ Ab ₂₆ Or ₁ (An ₇₄)	An ₇₀ Ab ₂₉ Or ₁	70
STL-50	An ₆₃ Ab ₃₆ Or ₁ (An ₆₄)	An ₆₈ Ab ₃₁ Or ₁	68
STL-100	An ₈₅ Ab ₁₅ Or ₀ (An ₈₅)	An ₇₄ Ab ₂₅ Or ₁	74
STL-138	An ₈₄ Ab ₁₅ Or ₀ (An ₈₄)	An ₇₁ Ab ₂₈ Or ₁	71
WAR-R0039	An ₄₇	An ₄₄ Ab ₅₂ Or ₄	46
WAR-R0519	An ₄₀₋₆₀	An ₅₂ Ab ₄₅ Or ₃	54
WAR-R1049	An ₅₄	An ₆₃ Ab ₃₄ Or ₂	65
WAR-R2624	An ₄₀₋₆₀	An ₅₆ Ab ₄₂ Or ₂	57
WAR-R3309	An ₆₀	An ₅₈ Ab ₄₀ Or ₂	59
WAR-R3319	An ₅₅₋₆₀	An ₄₆ Ab ₅₁ Or ₂	47

*Composition shown for Ward's samples does not include any modeled alkali end-members.

these types of mafic rocks, the alkali feldspar in the model results cannot be easily explained by a second phase. In comparing the measured and modeled spectra, RSL-9-94-12 and RSL-9-94-36, both exhibit a similar misfit near 1100 cm⁻¹ (Figure 3). This difference between the modeled and measured spectra in this wavelength region may indicate that the end-member suite does not include a mineral that is in the samples. Two likely components are glass and pigeonite, which were not included (glass) or were not available (pigeonite) as end-members at the time of the study. Both glass and pigeonite are common components in fine-grained extrusive mafic rocks, and both exhibit a strong spectral feature in the 1075–1100 cm⁻¹ region [Ramsey and Fink, 1999; Hamilton, this issue]. Future studies will examine the potential for improvement with these end-members.

In summary, 18 of 20 modeled feldspar compositions contained a significant volumetric majority of plagioclase components, as expected for these types of rocks. In 19 of 20 modeled feldspar compositions, the plagioclase components had An numbers between 45 and 85, in perfect accordance with those expected for mafic igneous rocks. Only two of 20 samples were modeled with prohibitively alkalic feldspar compositions. The two samples modeled with highly alkalic compositions demonstrate noticeable misfit in the ~1100 cm⁻¹ region of the spectrum, which serves as an indicator that some spectral feature is not being adequately modeled.

4.2.2. Comparison of average modeled feldspar composition to known composition. Feldspars from all five of the Stillwater (STL) cut rocks have been analyzed by electron microprobe, and ranges of An numbers for plagioclases in six of the remaining cut samples were estimated from thin sections by V.E.H. using the Michel-Lévy and Carlsbad-albite methods [Nesse, 1991]. (Two other cut surface samples were not measured because the feldspar in one comprised a fine-grained groundmass, and the twins in the grains of the other sample were too fuzzy to obtain estimates.) Only a minimum An number was estimated in the feldspars of the natural surface (RSL) rocks [Leighly, 1997]. The average feldspar compositions from the deconvolution are compared to the measured compositions in Table 5.

All of the cut STL samples have An numbers ranging from 64 to 85, as measured by microprobe analysis. The An numbers of the average model composition for these samples are 68–74, within 4–13 of the actual compositions. All of the modeled

compositions have a potassium component of Or₁, and the actual compositions are all Or₁ or less. The optically estimated An numbers of the remaining cut rocks are generally lower, from 40 to 60. The modeled plagioclase compositions for these samples range from 46 to 65. The modeled An numbers are within 1–11 of those estimated from the thin sections.

4.2.3. Model-derived pyroxene compositions: All rocks. Pyroxene compositions are defined by end-members wollastonite (Wo = CaSi₂O₆), enstatite (En = Mg₂Si₂O₆), and ferrosilite (Fs = Fe₂Si₂O₆). Compositions between the Mg and Fe end-members and with <5 mol % Ca are orthopyroxenes, and minerals in the solid solution series between Mg and Fe and containing ~40–50 mol % Ca are clinopyroxenes. Because there is virtually no solid solution between ortho- and clinopyroxene, modeled end members from these groups are kept separate and are not averaged together. Thus all modeled pyroxene compositions lie in valid ternary space. The model-derived weighted average compositions of orthopyroxene and clinopyroxene compositions are shown in Table 6. All 20 rocks in the study contain clinopyroxene, and 13 contain orthopyroxene. Of the modeled clinopyroxenes, average compositions range from Mg- and Ca-rich (diopside) to low-Ca and Fe-enriched (augite). All have Mg numbers, [Mg/(Mg + Fe)] × 100, greater than 57, which is reasonable for mafic and ultramafic igneous rocks. Among the orthopyroxenes, modeled Mg numbers range from 72 to 93, also reasonable for these types of rocks.

4.2.4. Comparison of average modeled pyroxene composition to known composition. Because of the difficulty in estimating pyroxene composition from optical analysis (with the exception of distinguishing between orthopyroxene and clinopyroxene), microprobe analyses are the best means of comparing modeled compositions to the true compositions in the rocks. Chemical data are available for all pyroxenes in the Stillwater (STL) cut rocks and for three of the natural surface (RSL) samples; the measured data are shown in comparison to the modeled compositions in Table 6. Measured and modeled ternary compositions are plotted in Figure 7. In terms of Mg number, modeled clinopyroxene compositions fall within 5–20 of the measured value; the worst case ($\Delta 20$) is correlated to a low modal percentage (6 vol %) of clinopyroxene in the model. As discussed above, modeled modes in the range around 5 vol % are suspect, so it is possible that at this low percentage, while the mineral selection may be broadly accurate, the accuracy of the modeled composition is poor. Excluding this case, modeled compositions fall within 5–14 Mg# of measured. Orthopyroxene compositions are modeled to within 25 Mg# of measured; however, a similarity to clinopyroxene results is observed in that the worst deviations from true composition are in the two cases where modeled opx modes are only 2 and 5 vol % of the rock. The modeled case with the largest deviation ($\Delta 25$) may also be affected by the available end-members. The measured composition of orthopyroxene in this sample (STL-50) is Mg₆₈, which is very close to the lower limit of Fe-rich compositions represented by the end-members. Part of the reason for the poor accuracy of this modeled composition, in addition to the low total mode, may be due to the lack of an appropriate end-member, or that the existing end-members cannot be combined to produce an average composition that would be closer to the real composition.

Excluding the two cases in which orthopyroxene is modeled at less than 5 vol % of the total rock, orthopyroxene composition is reproduced much more accurately than in the clinopy-

Table 6. Measured and Model-Derived Pyroxene Compositions

Sample	Measured Clinopyroxene	Modeled Clinopyroxene	Vol % Measured	Vol % Modeled	Measured Orthopyroxene	Modeled Orthopyroxene	Vol % Measured	Vol % Modeled
RSL-11-94-2	Wo ₄₄ En ₄₅ Fs ₁₁	Wo ₄₉ En ₃₇ Fs ₁₄	15	19	N/A	...	0	0
RSL-12-94-8	N/A	Wo ₄₈ En ₃₉ Fs ₁₃	20	13	N/A	...	0	0
RSL-4-95-23	N/A	Wo ₄₅ En ₄₃ Fs ₁₂	15	17	N/A	...	0	0
RSL-9-94-12	N/A	Wo ₄₆ En ₅₀ Fs ₄	25	13	Wo ₄ En ₇₆ Fs ₂₀	...	0	0
RSL-9-94-36	N/A	Wo ₄₆ En ₅₀ Fs ₄	15	22	N/A	...	0	0
RSL-9-94-41	Wo ₄₂ En ₄₃ Fs ₁₅	Wo ₄₆ En ₅₀ Fs ₄	15	13	N/A	Wo ₀ En ₉₃ Fs ₇ *	0	0
RSL-9-94-42	N/A	Wo ₅₀ En ₄₆ Fs ₅	15	12	N/A	...	0	0
STL-5	Wo ₄₆ En ₄₅ Fs ₁₀	Wo ₄₉ En ₄₅ Fs ₇	20	16	Wo ₃ En ₇₂ Fs ₂₅	Wo ₄ En ₇₂ Fs ₂₃	10	8
STL-20	Wo ₄₅ En ₄₄ Fs ₁₁	Wo ₅₀ En ₅₀ Fs ₀	5	6	Wo ₃ En ₇₃ Fs ₂₄	Wo ₄ En ₇₃ Fs ₂₃	15	11
STL-50	Wo ₄₅ En ₄₃ Fs ₁₂	Wo ₄₉ En ₄₇ Fs ₄	10	18	Wo ₃ En ₆₇ Fs ₃₁	Wo ₀ En ₉₃ Fs ₇	20	5
STL-100	Wo ₄₇ En ₄₇ Fs ₆	Wo ₅₀ En ₅₀ Fs ₀	15	15	Wo ₂ En ₈₂ Fs ₁₆	Wo ₁ En ₇₆ Fs ₂₂	15	14
STL-138	Wo ₄₄ En ₄₈ Fs ₈	Wo ₄₈ En ₅₀ Fs ₃	20	17	Wo ₂ En ₈₀ Fs ₁₈	Wo ₀ En ₉₃ Fs ₇	15	2
WAR-R0039	N/A	Wo ₄₄ En ₃₉ Fs ₁₇	40	45	N/A	Wo ₀ En ₉₃ Fs ₇ *	0	2
WAR-R0519	N/A	Wo ₄₇ En ₄₈ Fs ₅	15	11	N/A	Wo ₀ En ₉₃ Fs ₇ *	0	5
WAR-R1049	N/A	Wo ₄₄ En ₃₃ Fs ₂₃	28	21	N/A	Wo ₀ En ₉₀ Fs ₁₀ *	0	11
WAR-R1079	N/A	Wo ₄₆ En ₄₅ Fs ₉	35	36	N/A	...	0	0
WAR-R2624	N/A	Wo ₄₄ En ₃₉ Fs ₁₆	30	23	N/A	Wo ₀ En ₉₃ Fs ₇ *	10	7
WAR-R3309	N/A	Wo ₄₃ En ₅₀ Fs ₇ *	5	3	N/A	Wo ₃ En ₇₇ Fs ₂₀ *	10	9
WAR-R3319	N/A	Wo ₄₄ En ₂₈ Fs ₂₈ *	0	4	N/A	Wo ₀ En ₉₃ Fs ₇ *	30	0
WAR-R6479	N/A	Wo ₅₀ En ₄₈ Fs ₂	5	6	N/A	Wo ₂ En ₈₆ Fs ₁₂	85	79

*Only one end-member in model fit. N/A, not available.

roxenes; the differences in measured and modeled Mg number in the three samples with >5 vol % modal opx are only one, two, and six Mg#. Orthopyroxene solid solution compositions may be modeled with a higher degree of accuracy than clinopyroxenes due to the less complicated chemistry of the orthorhombic minerals. Work by *Hamilton* [this issue] has shown that variations in pyroxene emissivity spectra can be linked to not only Mg-Fe substitution in clinopyroxene but also to Ca abundance. Because the clinopyroxenes have this additional degree of compositional (and spectral) complexity, it may be more difficult to model their compositions as accurately as the orthopyroxenes in the absence of a wide range of end-member compositions along both the Mg-Fe and Ca-opx compositional trends. One possible remedy would be to include as many clinopyroxene end members as possible, increasing the number of end-members available to generate the model fit.

4.2.5. Summary: Reproduction of solid solution compositions. The modeled compositions of both plagioclase and pyroxene are typically within appropriate regions of the respective ternary compositional fields for these types of rocks. In three cases, large quantities (10–23 vol %) of alkali feldspar were included in model fits. The best explanation for these abundances may be that some spectral feature(s) in the rock spectra cannot be modeled with the end-members provided and that alkali feldspar is being added to the model fit incorrectly. Perhaps in an advanced strategy for modeling mafic and ultramafic rocks, these end-members should not be included (not an unreasonable suggestion, due to the rarity of alkali feldspar in these lithologies). A test of this would be to reapply the deconvolution after removing these end-members, and examining the resultant plagioclase compositions in comparison to the plagioclase compositions derived here. When average modeled compositions of plagioclase and pyroxene are compared to known chemistries, both plagioclase and pyroxene are generally modeled to within 10–15 An# or Mg# of the actual composition when present at greater than ~5 vol %. This result demonstrates that solid solution compositions in the feldspar and pyroxene series can be discriminated and modeled using a suite of end-members that combine to produce a com-

position similar to that contained in the rock. Orthopyroxene solid solution compositions tend to be modeled slightly more accurately than clinopyroxene compositions, possibly because the compositional space is two-dimensional (Mg-Fe), rather than three-dimensional as in the case of the clinopyroxenes (Mg-Fe-Ca).

4.3. Reproduction of Weight Percent Oxide Data From Modeled Modes

Classification of volcanic rocks is conventionally based on the bulk chemistry, in terms of the weight percentages of major oxides, of the rocks rather than the modal mineralogy. Therefore it is of interest to determine whether conversion of modes derived from thermal infrared spectra to weight percent (wt %) oxides provides an effective means of classifying volcanic samples. Weight percent oxide information for a rock can be calculated from the results of a sample deconvolution by converting the derived modes to oxides using the known oxide data for each of the model end members used in the model fit. However, it is important to recognize that the conversion from modal mineralogy to wt % oxides is a degradation of the mineralogical information and is necessarily based on the chemistries of the samples contained in the end-member mineral library used, not those in the measured rock. Furthermore, if there is a significant discrepancy between the modal abundances or solid solution chemistry returned by the model and those determined by optical or other methods (beyond the known error bounds of each method), the conversion of model-derived modes to bulk weight percent oxide will carry through this error. (Clearly, such a discrepancy could only be established in remotely acquired data if the model yields unrealistic solid solution compositions or there is significant misfit between the measured and modeled spectra, as described above.)

To test the accuracy of converting from mineral modes to wt % oxides, modal mineral data derived from the deconvolution of each rock were converted to weight percents of major oxides so that a comparison to the rocks' known bulk chemistry could be made. Once the deconvolution is applied and pro-

vides modal information about a sample, the oxide data for all end-members can be summed in proportion to the modal percentage of each end-member measured, thus producing a model derived bulk analysis. The following discussion compares the model-derived oxides to the actual bulk oxide data in terms of major oxides. Figure 8 shows the measured versus modeled oxide data for all 20 samples.

4.3.1. SiO₂. Silica content provides a general estimation of whether an igneous sample is mafic or felsic in overall composition. Mafic rocks typically have lower silica contents than felsic rocks, ranging from ~40–60 wt %. Felsic rocks generally have higher silica contents, ranging from 60 to 70 wt % SiO₂. Errors in silica content are low overall, ranging from 0.3 to 6.3% (average 2.5%), and the model-derived oxides are sufficient to distinguish these samples as mafic, ranging from 40 to 55% SiO₂. In all cases but one, silica is slightly overestimated, suggesting that overestimation of SiO₂ is not uniquely related to the surface texture, weathering, or alteration of the sample. Because the trend is apparent in virtually all of the samples, and because the percentages of error in these estimations are so small, it is difficult to pinpoint the mineral(s) in the deconvolution results that would produce the minor overestimations observed.

4.3.2. Al₂O₃. Errors in model-derived aluminum content exhibit a much larger spread than for silica, with errors averaging 8.2%. Aluminum content was overestimated in 80% of

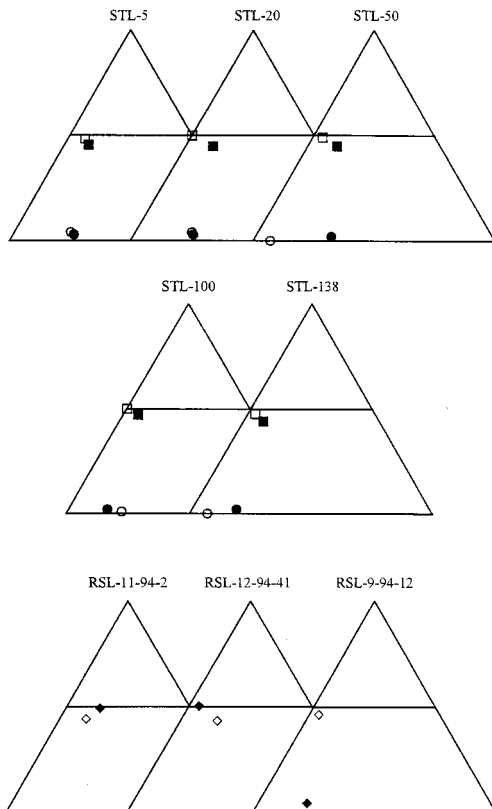


Figure 7. Ternary plots of measured (solid symbols) and modeled (open symbols) pyroxene compositions. The apex of each ternary represents the wollastonite end-member (Wo), the lower left corner is the enstatite end-member (En), and the lower right corner is the ferrosilite end-member (Fs). Circles denote orthopyroxene, and squares and diamonds denote high-Ca clinopyroxene.

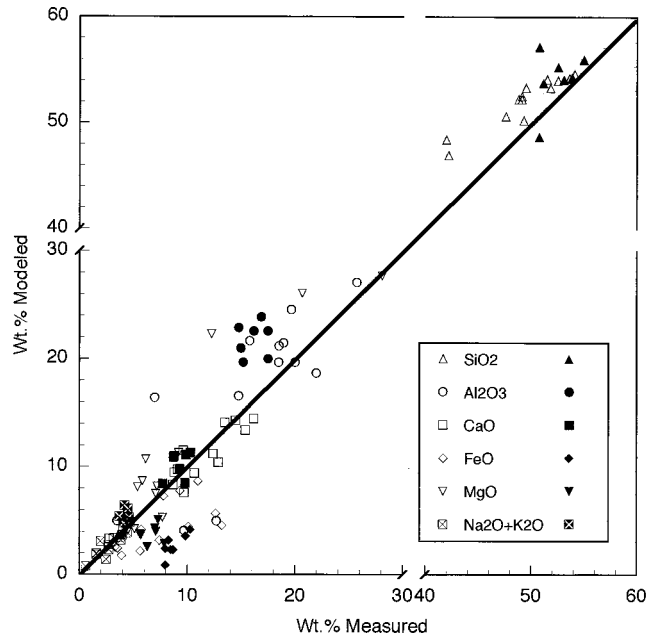


Figure 8. Comparison of measured and modeled weight percent oxides for all samples. Open symbols represent data for rocks analyzed on cut surfaces, and solid symbols represent data for rocks analyzed on natural surfaces. Some plot points represent more than one measurement.

the rocks (Figure 8). Relative to pyroxene and olivine, plagioclases are high in Al₂O₃, and the highest abundances of Al₂O₃ are associated with rocks having modal feldspar >65 vol %. Because of the abundance of Al₂O₃ in the Ca-rich varieties of plagioclase found in most of these rocks, slight overestimations of their modal percentages by the model, or errors in their solid solution compositions (i.e., more calcic than actual) may be responsible for the overestimation of Al₂O₃. However, comparison of effective model-derived plagioclase composition and actual composition show (Table 5) that derived compositions tend to be more sodic than actual, suggesting that errors in solid solution composition do not influence the rocks' total Al₂O₃ content as much as modal abundances do.

4.3.3. CaO. Calcium errors average 1.3%, with a range of ±0.2–2.6%. Absolute abundances of CaO range from 2 to 17 wt %. Unlike SiO₂ and Al₂O₃, CaO does not show a tendency to overestimation, with 11 samples falling above the perfect fit (1:1) line and nine samples below (Figure 8). The greatest contributions to calcium abundance in these rocks are plagioclase feldspar and clinopyroxene (as well as some amphiboles and carbonate, if significant volumetrically). The fairly good overall fits to CaO indicate that these two minerals are not only well modeled in abundance (particularly clinopyroxene versus orthopyroxene) but also in terms of solid solution composition (most significant in plagioclase), and this is supported by the generally good correlation (±10–15 Mg# or An#) described above between the measured and modeled plagioclase and pyroxene compositions (Tables 5 and 6).

4.3.4. FeO. FeO abundances are small in these rocks, varying from 3.1 to 13.2 wt %, with an average of 7.9%. Errors in modeled FeO range widely from 0.2 to 8.6%, with an average of 4.2%. The model-derived wt % oxide is underestimated in all cases (Figure 8). In terms of percent error, these are large errors; in terms of absolute error, these modeled values rep-

resent Δ wt % of 5.2–7.2. For these rocks, FeO is most important in pyroxenes, olivines, hornblendes, and biotite, although the latter two minerals are not commonly modeled as being present in these rocks. For applications where relative FeO content is important at the few percent level, these modeled values contain prohibitive error. For applications where FeO is important as some portion of the total rock chemistry (i.e., at the 10–20+ wt % level), these errors may be less significant. Because olivine modes (measured and modeled) are typically very low in these rock samples (<10 vol %), the derived FeO is dominated by pyroxene chemistry. Low FeO suggests that solid solution compositions are being modeled as more magnesian than they really are. This is, in fact, the case for all five of the Stillwater (STL) cut surface samples, and two of the three cases in which pyroxene composition is known for natural surface samples (refer to section 4.2 above).

4.3.5. MgO. Magnesium is overestimated in seven of the rock samples and underestimated in 10 samples (three samples were modeled to within 1 wt % of the measured value). Errors range from 0.2 to 8.6%, with an average of 2.7%. Total measured MgO in these samples ranges from 4 to 28 wt %, with most samples (85%, 17 out of 20) having MgO contents <10 wt % (Figure 8). The minerals contributing most to total MgO are pyroxene, olivine, amphibole, mica, and serpentine. MgO in all of the natural surface samples is underestimated (although not as much as FeO is), but the largest deviations from the measured MgO content occur in three cut surface samples: WAR-R0039, WAR-R1049, and WAR-R1079. All three samples have large (40–92 vol %) modeled modal percentages of Mg-bearing minerals, and pyroxene modes ranging from 32 to 47 vol %. As discussed above, most modeled pyroxene compositions are 10–15 Mg# more magnesian than the actual composition; at large modeled modes, these differences should be observed in the oxides as an overabundance of MgO, as is the case.

4.3.6. FeO + MgO. If all errors in FeO and MgO wt % oxide are derived from less than ideal modeling of solid solution compositions, then the sum of the modeled FeO and MgO would be expected to show a much closer correlation with the measured sum of the two oxides than either of the two individual comparisons. However, natural surface samples would still plot significantly below the ideal fit line, having 48–69% less FeO + MgO than the measured value. This observation suggests that mafic minerals are somehow underestimated in general in this group of rocks. Olivine modes are all underestimated, and in one case, a measured mode of 10 vol % was not identified at all in the deconvolution. Because olivine is an Mg-Fe mineral, this consistent underestimation of olivine contributes to the low FeO + MgO of the natural surface samples. Additionally, several of the natural surface samples were modeled as containing clays, presumably due to surficial contamination, and these rocks show the highest deviations from the measured FeO + MgO. Clays contain little FeO and MgO and may explain the lack of magnesium and iron in the derived oxides. Because the spectra used in the model fits are averages of two to three spots on the exterior of each sample, surficial contamination will influence the model-derived modes, whereas such contamination does not strongly influence a traditional bulk analysis. Opaques were identified only in two of the natural surface samples, and at abundances of only 2 vol %; thus the lack of opaque mineral spectral end-members in the model is probably not responsible for the FeO + MgO deficiency in these rocks. The only sample for which the

opaque minerals may have been significant is WAR-R0039, which was estimated from thin section analysis to contain 5–7 vol % opaque minerals. Because this mode could not be modeled by any of the provided spectral end-members, one or more of the modes in the model fit are inflated slightly. If one of the Mg/Fe mineral modes were to be reduced and replaced by a Fe-oxide, the FeO + MgO modeled would probably match the measured value more closely.

4.3.7. Na₂O + K₂O. Because alkali abundances are generally very low in mafic and ultramafic rocks (<5–7 wt %), and because they are often considered as a sum, they will be considered together here, plotted in Figure 8. Errors in the model range from 0.2 to 2.1%, with an average of 0.9%. Na₂O + K₂O is overestimated by >1 wt % in four samples, all of which contain significant amounts of alkali feldspar or albite, and/or illite clay in the modeled modes. These minerals have significant abundances of alkalis, and because we believe that the alkali feldspars in particular were modeled erroneously, these modeled minerals are probably the source of the inflated alkali oxides. One sample's alkali value was underestimated by >1 wt % (WAR-R0039); the model-derived modes are dominated by mafic minerals and contain ~40 vol % augite. The samples fit by the model are both very low in alkalis, and because of their large modal abundance, probably underrepresent the amount of Na₂O + K₂O actually present in the sample.

5. Classification of Rocks From Model-Derived Modes

Although classification schemes are generally somewhat arbitrary, they are based on relatively important chemical and/or mineralogical trends that provide insight into the conditions during rock formation, and even a general understanding of the mineralogy or chemistry of a sample provides a great deal of information about the rock. Unknown rock types are commonly classified by their modal mineral abundances or chemistries on determinative plots. For plutonic rocks, classifications are commonly plotted on ternary diagrams on the basis of the relative abundance of the three major minerals in the sample. Plotting the model-derived modal abundances versus the known abundances of the plutonic rocks studied shows how well a sample can be classified based on deconvolution results. Figure 9 shows the known compositions of the cut surface, intrusive samples in comparison to the model derived modes of the three major minerals, plagioclase, orthopyroxene, and clinopyroxene. Five of the eight modeled rock compositions plot within 5% of the known composition (WAR-R6479, WAR-R3309, STL-5, STL-20, and STL-100), two plot within 20% (STL-50 and STL-138), and one plots within 30% (WAR-R3319).

Two of the three samples with $\geq 20\%$ error plot in a different compositional field than is actually represented by the rock (STL-138 and WAR-R3319). The error in both cases is due to the underestimation of orthopyroxene in the modeled modes. It is important to note that the compositional space of gabbroic rocks is vast, and that significant errors in relative modal mineralogy determined by the deconvolution could go undetected if no other analysis is available. However, it is an indication of the power of the deconvolution technique that of these eight samples, all plot on the diagram and in approximately the correct region of the ternary.

Volcanic rocks can be classified as basalt, basaltic andesite, dacite, etc., by plotting SiO₂ content versus alkalis (Na₂O +

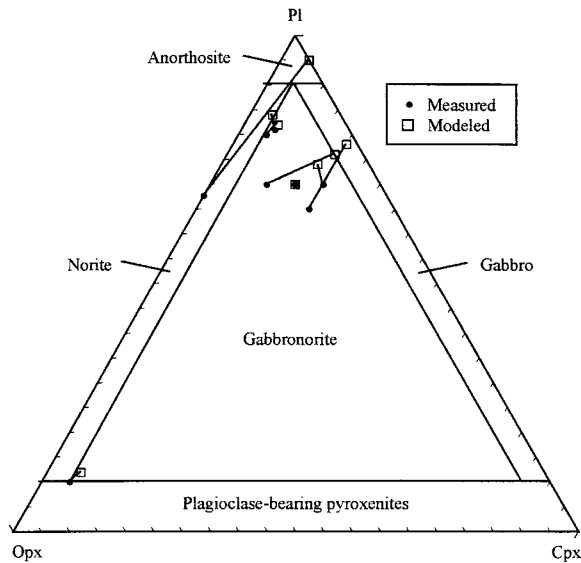


Figure 9. IUGS classification diagram for plutonic rocks. Dots represent measured compositions, and open symbols represent compositions determined by linear deconvolution of thermal emission spectra.

K_2O) [Le Bas *et al.*, 1986]. Eleven of the 20 samples studied are volcanic; their measured and model-derived SiO_2 and $Na_2O + K_2O$ values are plotted in Figure 10. As in the case of the plutonic samples, deconvolution results place all modeled compositions on the diagram and in the approximately correct compositional fields. Seven of the 11 samples do not quite fall in the actual classification space of the sample based on measured bulk composition. Five of the seven reclassifications result primarily from overestimation of SiO_2 , one results primarily from overestimation of alkali content, and one is the result of gross overestimation of both SiO_2 and alkalis. The classification fields on this diagram are narrowly defined, and while many of the modeled compositions fall outside the known classes, the classifications are still reasonably accurate in the broader sense of a totally unknown rock, as might be observed from a remote sensing platform. If a correction to model-

derived SiO_2 were applied based on the overestimation trend observed above, several of these rocks could be plotted more accurately. Because the total wt % of the alkalis is generally very small in these rocks, a correction may be more difficult to determine. It may be necessary to simply place error bounds on the alkali content that are equal to the average error of the model-derived $Na_2O + K_2O$, in this case, $\pm 0.9\%$. Such error bounds allow the model-derived points in the basaltic trachyandesite and trachyandesite fields to overlap the more accurate basaltic andesite and andesite fields.

Although some of the rocks did not fall into narrowly defined nomenclature boundaries on the basis of wt % SiO_2 and $Na_2O + K_2O$ alone, it is important to remember that this does not necessarily prevent their identification. Spectral shapes of unknown samples can always be compared to libraries of rock spectra with known compositions. As bulk compositions change, so does the mineralogy, and although this might not be fully reflected in a plot of SiO_2 versus alkalis, it will be apparent in the spectrum of the sample and the modeled mineralogy, again emphasizing the necessity for developing modal classification schemes for extrusive rocks [Wyatt *et al.*, 1999].

6. Determination of Modal Mineralogy at Decreased Spectral Sampling

Because the results presented above reflect the success of the deconvolution technique with high SNR, high spectral resolution laboratory data, equally accurate results should not be expected with remotely acquired data, which typically have lower SNR and spectral resolution, must be corrected for atmospheric contributions, and represent a variety of surface textures, including bedrock, and coarse and fine regolith. Dusty surfaces dominated by volume scattering likely will not be easily deconvolved using this technique; however, the results of this study should be applicable to solid surfaces and particulate materials with effective diameters greater than $\sim 65 \mu m$. We base this lower limit on work by Hamilton [1999a, b] that demonstrates that the spectral signatures of crushed rock samples down to particle sizes of $\sim 65 \mu m$ (the onset of volume scattering) are changed only in contrast (i.e., the addition of blackbody), not in shape, from 1300 to 400 cm^{-1} . Thus the

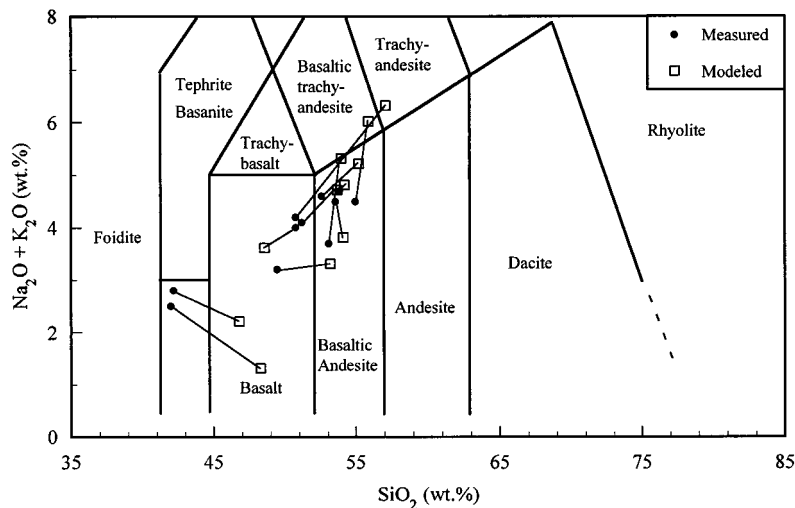


Figure 10. Chemical classification scheme for volcanic rocks. Symbols are the same as in Figure 9 (After Le Bas *et al.* [1986]; permission for use granted by Oxford University Press.)

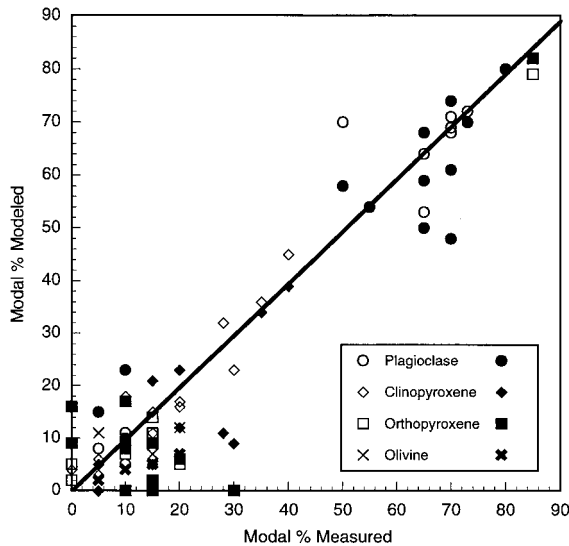


Figure 11. Comparison of optical and model-derived modes for major/primary minerals in cut rock samples. Open symbols represent data at 2 cm^{-1} sampling, and solid symbols represent data at 10 cm^{-1} sampling. Some plot points represent more than one measurement.

linear deconvolution technique will provide significant insight into the major component mineralogy of solid and many particulate surfaces.

As an example, library end-member mineral spectra and spectra of samples with cut surfaces were convolved to 10 cm^{-1} spectral sampling, with bandpasses corresponding to the 10 cm^{-1} sampling mode of the Mars Global Surveyor Thermal Emission Spectrometer (TES) [Hamilton, 1999c]. (Natural surface samples demonstrated deconvolution accuracies comparable to those of cut surfaces and are not shown for the sake of clarity.) Linear deconvolution results at this resolution demonstrate a slight increase in the spread for samples with modal abundances $\geq 10\text{ vol } \%$; nonetheless, 29 of 33 modeled modes (88%) are within 15 vol % (the maximum estimated error) of the optically determined mode (Figure 11). This represents an increase in uncertainty of about 5 vol % over the 2 cm^{-1} sampling results described in section 4.1 in which 88% of the $\geq 10\text{ vol } \%$ modes were modeled to within 10 vol % of the optical mode. All data points except one lie within 20 vol % of the optical mode, indicating that gross errors do not result with decreased spectral resolution. As a further indication of consistency between results at differing spectral resolutions, it is interesting to note that the 30 vol % orthopyroxene measurement not detected at 2 cm^{-1} sampling was not detected at 10 cm^{-1} sampling either. For minerals with optical modes $< 10\text{ vol } \%$, 75% were determined to within the optical error of $\pm 5\text{ vol } \%$.

7. Conclusions

1. Linear deconvolution of thermal infrared emission spectra (acquired on both cut and natural surfaces) successfully identifies the primary and secondary minerals in a suite of mafic and ultramafic intrusive and extrusive igneous rocks.

2. The vast majority (92%) of modal mineral abundances derived from thermal infrared spectra agree with optically derived modes to within the error of the optical analyses, regard-

less of whether the spectrum was acquired on a cut or natural surface. In cases where there is a significant deviation from the measured mode of a mineral, the thin section may not be representative of the surface analyzed spectrally. Alternatively, the modeled modes may contain components that are indicative of mineral alteration, which are easily underestimated or not observed in thin section analysis when such analysis is aimed at describing the primary minerals in a sample.

3. Model-derived modes belonging to the feldspar solid solution series may be combined to derive a single, weighted average composition along that solid solution series, which may then be used to estimate the "realness" of the modeled composition. Of 20 average feldspar compositions, only four do not plot in the compositional space of any feldspar. Of these, only two occur as geologically significant modes and are associated with spectral misfit around $\sim 1100\text{ cm}^{-1}$. This observation suggests that the alkali feldspar components in these two cases do not represent the true feldspar compositions of these rocks but are substituted for a mineral in the rocks that is not included in the end-member mineral spectra. Fifteen of the remaining modeled compositions fall within plagioclase compositional fields that are characteristic of mafic and ultramafic rocks, indicating that the deconvolution is not randomly fitting feldspars but is distinguishing spectral variation among members of the plagioclase series.

4. Five feldspars and 13 pyroxenes have compositional data available that were compared to the effective compositions of these minerals as derived from the spectral deconvolution. The effective compositions of both pyroxenes and feldspars modeled at $> 5\text{ vol } \%$ are generally within 10–15 Mg# (An#) of the compositions measured by microprobe analysis. The highest deviations from the measured compositions are correlated with low modeled abundances, which tend to be suspicious based on the known limitations of the deconvolution modeling. In only one case was orthopyroxene in a rock misidentified as clinopyroxene.

5. Modal mineralogical data obtained from thermal emission spectra can be used to broadly classify unknown plutonic rocks on a determinative plot. Conversion of spectrally derived modal data to wt % oxides for rock type classification is very promising; classifications are generally accurate and can be supplemented with the full modal mineralogical information provided by the model. Spectra of all unknown rocks may and should also be compared to library rock spectra, especially in cases where spectral data are remotely acquired. Future additions to the end-member set (basaltic glasses and pigeonite) should improve model fits and subsequent classifications.

6. Convolution of laboratory data to spectral resolutions typical of remote sensing instruments does not produce significantly degraded deconvolution results. Almost 90% of modes $\geq 10\text{ vol } \%$ are modeled to within the error associated with optical analysis. These results are probably a best case example, as remote sensing data are likely to have lower SNR than laboratory data, as well as additional atmospheric components that require removal prior to deconvolution. However, these additions are unlikely to introduce prohibitively large effects, and the deconvolution technique should produce viable results at the $> 10\text{--}15\text{ vol } \%$ level [Christensen *et al.*, this issue (a)].

Acknowledgments. Thanks to Will Stefanov (Department of Geology) and Jim Clark (Department of Chemistry) for valuable assistance in obtaining optical analyses and electron microprobe measurements. Thanks also to Bob Leighty and Kim Feely for sharing personal

notes and observations regarding the RSL samples, as well as the samples and their spectra. We also appreciate the donation of Stillwater Complex samples by I. S. McCallum; these samples arrived with the following sample numbers, which were shortened in the text: STL-100, S-50, 88-138, 93-20, and 94-5. The National Museum of Natural History at the Smithsonian Institution kindly provided many pyroxene samples used in this research, which can be identified in Table 3 by sample numbers beginning NMNH-. We appreciate the efforts of T. Hiroi and an anonymous reviewer for providing helpful feedback on this manuscript. This research was supported by a National Physical Science Consortium Fellowship with stipend support from the Jet Propulsion Laboratory (V.E.H.) and NASA grant NAGW 943 (V.E.H. and P.R.C.).

References

- Christensen, P. R., and S. T. Harrison, Thermal infrared emission spectroscopy of natural surfaces: Application to desert varnish coatings on rocks, *J. Geophys. Res.*, **98**, 19,819–19,834, 1993.
- Christensen, P. R., J. L. Bandfield, M. D. Smith, and V. E. Hamilton, Identification of a basaltic component on the Martian surface from Thermal Emission Spectrometer data, *J. Geophys. Res.*, this issue (a).
- Christensen, P. R., J. L. Bandfield, V. E. Hamilton, D. A. Howard, M. D. Lane, J. L. Piatek, S. W. Ruff, and W. L. Stefanov, A thermal emission spectral library of rock forming minerals, *J. Geophys. Res.*, this issue (b).
- Feely, K. C., Quantitative compositional analysis of igneous and metamorphic rocks using infrared emission spectroscopy, M.S. thesis, 169 pp., Ariz. State Univ., Tempe, 1997.
- Feely, K. C., and P. R. Christensen, Quantitative compositional analysis using thermal emission spectroscopy: Application to igneous and metamorphic rocks, *J. Geophys. Res.*, **104**, 24,195–24,210, 1999.
- Hamilton, V. E., Thermal infrared emission spectroscopy of the pyroxene mineral series and pyroxene-bearing lithologies, Ph.D. dissertation, 214 pp., Ariz. State Univ., Tempe, 1998.
- Hamilton, V. E., The effect of particle size on rock spectra in the thermal infrared: Implications for TES data analysis, *Lunar Planet. Sci. [CD-ROM]*, **XXX**, abstract 2001, 1999a.
- Hamilton, V. E., Particle size effects in particulate rock samples: Implications for Thermal Emission Spectrometer (TES) data analysis in high-albedo regions on Mars, in *Fifth International Conference on Mars [CD-ROM]*, abstract 6159, Lunar and Planet. Inst., Houston, Tex., 1999b.
- Hamilton, V. E., Linear deconvolution of mafic igneous rock spectra and implications for interpretation of TES data, *Lunar Planet. Sci. [CD-ROM]*, **XXX**, abstract 1825, 1999c.
- Hamilton, V. E., Thermal infrared emission spectroscopy of the pyroxene mineral series, *J. Geophys. Res.*, this issue.
- Hamilton, V. E., P. R. Christensen, and H. Y. McSween Jr., Determination of Martian meteorite lithologies and mineralogies using vibrational spectroscopy, *J. Geophys. Res.*, **102**, 25,593–25,603, 1997.
- Hunt, G. R., and R. K. Vincent, The behavior of spectral features in the infrared emission from particulate surfaces of various grain sizes, *J. Geophys. Res.*, **73**, 6039–6046, 1968.
- Le Bas, M. J., R. W. Le Maitre, A. Streckeisen, and B. Zanettin, A chemical classification of volcanic rocks based on the total alkali-silica diagram, *J. Petrol.*, **27**, 745–750, 1986.
- Leighty, R. S., Neogene tectonism and magmatism across the Basin and Range–Colorado Plateau boundary, central Arizona, Ph.D. dissertation, 1069 pp., Ariz. State Univ., Tempe, 1997.
- Lyons, R. J. P., Analysis of rocks spectra by infrared emission (8–25 μm), *Econ. Geol.*, **60**, 715–736, 1965.
- McBirney, A. R., *Igneous Petrology*, 2nd ed., 508 pp., Jones and Bartlett, Boston, Mass., 1993.
- McCallum, I. S., The Stillwater Complex, in *Layered Intrusions*, edited by R. G. Cawthorn, 531 pp., Elsevier, New York, 1996.
- Moersch, J. E., and P. R. Christensen, Thermal emission from particulate surfaces: A comparison of scattering models with measured spectra, *J. Geophys. Res.*, **100**, 7465–7477, 1995.
- Nesse, W. D., *Introduction to Optical Mineralogy*, 335 pp., Oxford Univ. Press, New York, 1991.
- Ramsey, M. S., Quantitative analysis of geological surfaces: A deconvolution algorithm for midinfrared remote sensing data, Ph.D. dissertation, 276 pp., Ariz. State Univ., Tempe, 1996.
- Ramsey, M. S., and P. R. Christensen, Mineral abundance determination: Quantitative deconvolution of thermal emission spectra, *J. Geophys. Res.*, **103**, 577–596, 1998.
- Ramsey, M. S., and J. H. Fink, Estimating silicic lava vesicularity with thermal remote sensing: A new technique for volcanic mapping and monitoring, *Bull. Volcanol.*, **61**, 32–39, 1999.
- Ruff, S. W., Quantitative thermal infrared emission spectroscopy applied to granitoid petrology, Ph.D. dissertation, 234 pp., Ariz. State Univ., Tempe, 1998.
- Ruff, S. W., P. R. Christensen, P. W. Barbera, and D. L. Anderson, Quantitative thermal emission spectroscopy of minerals: A laboratory technique for measurement and calibration, *J. Geophys. Res.*, **102**, 14,899–14,913, 1997.
- Salisbury, J. W., and J. W. Eastes, The effect of particle size and porosity on spectral contrast in the mid-infrared, *Icarus*, **64**, 586–588, 1985.
- Salisbury, J. W., and A. Wald, The role of volume scattering in reducing spectral contrast of reststrahlen bands in spectra of powdered minerals, *Icarus*, **96**, 121–128, 1992.
- Sharp, T. G., R. J. Stevenson, and D. B. Dingwell, Microlites and “nanolites” in rhyolitic glass: Microstructural and chemical characterization, *Bull. Volcanol.*, **57**, 631–640, 1996.
- Taylor, L. A., A. Patchen, D.-H. S. Taylor, J. G. Chambers, and D. S. McKay, X-ray digital imaging and petrography of lunar mare soils: Data input for remote sensing calibrations, *Icarus*, **124**, 500–512, 1996.
- Thomson, J. L., and J. W. Salisbury, The mid-infrared reflectance of mineral mixtures (7–14 μm), *Remote Sens. Environ.*, **45**, 1–13, 1993.
- Vincent, R. K., and F. Thompson, Spectral compositional imaging of silicate rocks, *J. Geophys. Res.*, **17**, 2465–2472, 1972.
- Walter, L. S., and J. W. Salisbury, Spectral characterization of igneous rocks in the 8- to 12- μm region, *J. Geophys. Res.*, **94**, 9203–9213, 1989.
- Wyatt, M. B., V. E. Hamilton, H. Y. McSween Jr., P. R. Christensen, A. Patchen, and L. A. Taylor, Comparison of microprobe and thermal emission spectroscopy derived modal mineralogies of basalt and andesite, *Lunar Planet. Sci. [CD-ROM]*, **XXX**, abstract 1754, 1999.

P. R. Christensen and V. E. Hamilton, Department of Geology, Box 871404, Arizona State University, Tempe, AZ 85287-1404. (hamilton@tes.la.asu.edu)

(Received June 10, 1999; revised September 7, 1999; accepted September 9, 1999.)

